UNIVERSITY OF CALIFORNIA,
IRVINE

Developing Optical Biometrics Using Optical Coherence Tomography for Medical Screening and Diagnosis

DISSERTATION

submitted in partial satisfaction of the requirements
for the degree of

DOCTOR OF PHILOSOPHY

in Biomedical Engineering

by

Andrew Emon Heidari

Dissertation Committee:
Professor Zhongping Chen, Chair
Professor Michelle Digman
Professor Bernard Choi

2018

DEDICATION

To

My loving family,

particularly my parents Narges and Ryan Heidari,

and my supportive friends and colleagues,

in recognition of their persistent support and care through my highs and lows

accompanied by the rigor of graduate school.

TABLE OF CONTENTS

LIST OF FIGURES

LIST OF TABLES

TABLE OF ABBREVIATIONS

OCT	Optical coherence tomography
OSCC	Oral squamous cell carcinoma
CT	Computed tomography
US	Ultrasound
MRI	Magnetic resonance imaging
VAP	Ventilator associated pneumonia
TD-OCT	Time domain optical coherence tomography
FD-OCT	Fourier domain optical coherence tomography
SS-OCT	Swept source optical coherence tomography
SD-OCT	Spectrometer based optical coherence tomography
FLIM	Fluorescence lifetime imaging
SNR	Signal to noise ratio
CCD	Charge coupled device
SEM	Scanning electron microscopy
ICU	Intensive care units
EtOH	Ethyl Alcohol
VSCEL	Vertical-cavity surface-emitting laser
NADH	Nicotinamide adenin dinucleotide
FAD	Flavin adenine dinucleotide
FD-FLIM	Frequency domain fluorescence lifetime imaging
TD-THz	Time domain terahertz spectroscopy

2D	Two dimensional
3D	Three dimensional
P1	Pseudomonas aeruginosa
SM	Stenotrophomonas maltophilia
RM	Rothia mucilaginous
SS	Streptococcus salvarius
LMIC	Low and middle-income countries
OPML	Oral potentially malignant lesions
GRIN	Gradient refractive index
ROI	Region of interest
PPV	Positive predictive value
NPV	Negative predictive value
COE	Conventional oral examination
AGA	Androgenic alopecia
MPHL	Male pattern hair loss
FPHL	Female pattern hair loss
AA	Alopecia areata

ACKNOWLEDGMENTS

I would like to express the deepest gratitude towards my advisor Professor Zhongping Chen that supported my ambition to try new things even though they were outside of his specific expertise. For his constant mentorship where I developed my investigative techniques drive and motivation needed to succeed in research. Having him as an advisor has not improved me as a researcher but showed me the reward of perseverance and working on your weaknesses.

I would like to thank the clinical physicians that have mentored me on my translational research projects. Specifically, I would like to thank Dr. Matthew Brenner, Dr. Brian Wong, Dr. William Armstrong, Dr. Tjoa Tjosen, Dr. Petra-Wilder Smith, Dr. Natasha Mesinkovska, and Dr. Ralph Clayman. Thank you for inspiring and supplementing my interest and fascination with the human body translational research. They have all kindly welcomed the use of new technologies into their practice. They have fostered a very enriching environment of learning and discovery, which has allowed me to use my engineering experience to make efforts to improve patient care.

Lastly, I would like to thank my fellow lab mates that support me through all the good and bad experiences through graduate school. I grew very close to my lab mates to the point where I felt closer to them than some of my blood relatives. Thank you to Rachel Qu, Yusi Miao, Joe Jing, Danny Chou, and Yan Li for making my graduate school experience memorable.

I would like to acknowledge the following funding sources that have supported this research: NIH UL1 TR000153, NIH UH2 EB022623, NIH R03 EB014852, P41-EB002182,

P41-EB015890, and the Department of Biotechnology, India. sanction number -
BT/MB/LCMD/04/2012.

CURRICULUM VITAE

Andrew Emon Heidari

2010 B.S., Biomedical Engineering University of California Irvine, Irvine, California

2016 M.S., Biomedical Engineering University of California Irvine, Irvine, California

2018 Ph.D., Biomedical Engineering University of California Irvine, Irvine, California

FIELD OF STUDY

Biophotonics and Biomedical Imaging

JOURNAL PUBLICATIONS

1. **Heidari AE**, Sunny SP, James BL, Lam T, Tran AV, Ravindra DR, Uma K, Praveen BN, Suresh A, Kuriakose MA, Chen Z, Wilder-Smith P. Novel Optical Coherence Tomography Probe for Oral Cancer Screening and Triage in a Low Resource Setting. Journal of Oral Oncology. Manuscript in Submission 2018

2. Li Y, Jing JC, **Heidari AE**, Zhu J, Qu Y, Chen Z. Intravascular Optical Coherence Tomography for Characterization of Atherosclerosis with a 1.7 Micron Swept-Source Laser. Scientific Reports. 2017;7:14525. doi:10.1038/s41598-017-15326-4.

3. **Heidari AE**, Moghaddam S, Truong KK, Chou L, Genberg C, Brenner M, Chen Z. Visualizing biofilm formation in endotracheal tubes using endoscopic three-dimensional optical coherence tomography, J. Biomed. Opt. 2015; 20(12) http://dx.doi.org/10.1117/1.JBO.20.12.126010

4. Sharma GK, Ahuja GS, Wiedmann M, Osann KE, Su E, **Heidari AE,** Jing JC, Qu Y, Lazarow F, Wang A, Chou L, Uy CC, Dhar V, Cleary JP, Pham N, Huoh K, Chen Z, Wong BJF. Long-Range Optical Coherence Tomography of the Neonatal Upper Airway for Early Diagnosis of Intubation-related Subglottic Injury. American Journal of Respiratory and Critical Care Medicine. 2015;192(12):1504-1513. doi:10.1164/rccm.201501-0053OC.

5. Lusch A, Leary R, **Heidari AE**, Liss MA, Okhunov Z, Perez-Lanzac De Lorca A, Huang J, Wikenheiser J, Landman J. Intrarenal and Extrarenal Autonomic Nervous System Redefined. The Journal of Urology. 2014; 191(4):1060-1065

6. Robertson C, **Heidari AE**, Chen Z, George S. Mechanical analysis of arterial plaques in native geometry with OCT wall motion analysis. Journal of Biomechanics. 2014;47(3):755-758

7. Lin JL, Yau AY, Boyd J, Hamamoto A, Su E, Tracy L, **Heidari AE**, Wang AH, Ahuja G, Chen Z, and Wong B.J. Real-Time Subglottic Stenosis Imaging Using Optical Coherence Tomography in the Rabbit. JAMA Otolaryngol Head Neck Surgery. 2013;139(5):502-509

8. Lee SW, **Heidari AE**, Yoon D, Mukai D, Tirunelveli R, Mahon S, Yin J, Liu G, Chen Z, and Brenner M. Quantification of airway thickness changes in smoke-inhalation injury using in-vivo 3-D endoscopic frequency-domain optical coherence tomography. Biomedical Optics Express. 2011; 2(2):243

9. Li Q, Huang S, **Heidari AE**, Dai C, Zhu J, Zhang X, Chen Z. Automatic airway wall segmentation and thickness measurement for long-range optical coherence tomography images, Proc. SPIE 9697, Optical Coherence Tomography and Coherence Domain Optical Methods in Biomedicine XX, 96973B. 2016; http://dx.doi.org/10.1117/12.2214605

ABSTRACT OF THE DISSERTATION

Developing Optical Biometrics Using Optical Coherence Tomography
for Medical Screening and Diagnosis

By

Andrew Emon Heidari

Doctor of Philosophy in Biomedical Engineering

University of California, Irvine, 2018

Professor Zhongping Chen, Chair

Optical coherence tomography (OCT), a non-invasive, high-resolution imaging modality, has seen an increasing role as a clinical diagnostic, screening, and therapeutic imaging method over the years. Medical specialties such as ophthalmology, interventional cardiology and gastroenterology have been able to take full advantage of OCT's minimally invasive near-cellular depth resolution to stage and diagnose different disease states and medical conditions. Although we have seen a wide spread use of OCT in the aforementioned specialties, there remains a plethora of medical specialties that could potentially benefit from the use of a non-invasive, high-resolution imaging modality. This thesis concentrates on developing the use of OCT and analytical image processing methods to address clinical unmet needs in interventional pulmonology, head and neck cancer and dermatology. The work presented will specifically discuss nosocomial ventilator associated pneumonia, oral squamous cell carcinoma (SCC), and androgenic alopecia (AA) respectively.

Each medical condition studied required a unique imaging system and imaging probe to properly assess the presented clinical need. Ventilator associated pneumonia (VAP) utilized a high-speed Fourier domain OCT (FD-OCT) imaging system with side-viewing probe, a microscope-based fluorescence lifetime imaging (FLIM) system, and a bench top terahertz spectroscopy system. Using the three imaging modalities, the macroscopic structure of bacterial biofilm in-situ as well as biofilm bacterial phenotype composition could be resolved. OSCC required the development of a portable low-cost spectral domain OCT(SD-OCT) imaging system and low-profile forward viewing scanning probe to transport the system overseas to Bangalore, India where oral cancer has a high prevalence. Using intensity-based OCT as compared to the histology gold standard, differences between normal, dysplastic and malignant oral mucosa were determined. Lastly, androgenic alopecia better known as male or female pattern baldness, utilized a larger 3D scanning hand held microscope probe that provided a wide field of view yet a high lateral resolution to observe differences in hair shaft and hair follicle structure between varying stages of balding.

Structural intensity-based OCT biomarkers are effective in analyzing various disease conditions, as evidence by the clinical OCT imaging applications. These biomarkers provide a means of assessing and staging the state of the medical condition in the spectrum between normal and abnormal. With such an imaging tool and outlook, physicians could further guide medical intervention, determine treatment efficacy and monitor disease progression.

Chapter 1

Introduction

1.1 Clinical Imaging and Current Limitations of Imaging Technology

In an ideal world, we would be able to diagnose and treat patients without any harmful side effects. Imaging, which is widely used in every day medical practice, is one attempt at that goal. We can see within the body without the need for surgery or other invasive procedures. Imaging aids in the differential diagnosis of patients when a physician is suspicious of a condition or when obvious physical exam findings are not evident. It also aids the surgeon with operative planning, and in monitoring disease progression and resolution. Used therapeutically, imaging can guide interventional minimally invasive procedures, providing vision and contrast to the doctor.

Current imaging methods include a wide variety of modalities, some able to resolve structures on a macro scale and others on a microscopic scale, some able to resolve depth related information with high resolution, some more precise, and some more invasive than others. Common types used clinically to provide structural and functional information include computed tomography (CT), magnetic resonance imaging (MRI), ultrasound (US), and x-ray, among others[1]. These imaging modalities provide powerful information on advanced disease processes, as they image the human body on a macro organ scale. The resolutions of these imaging modalities are not fine enough to resolve micro-structure changes evident at an early stage of disease development. In addition, some of these methods

can be harmful, such as CT or x-ray which utilize harmful radiation, carrying a risk of causing cancer many years or decades later, particularly with repeat or large exposure. However, the introduction of OCT a minimally-invasive, high-resolution imaging modality, allowed depth resolved structural and functional information that is sensitive to less advanced pathological changes to tissue to be ascertained.

1.2 Optical Coherence Tomography

Optical coherence tomography utilizes low-coherent near-infrared laser light in a Michelson based interferometer to generate tomographic depth resolved scattering and absorption information of biological samples. Often, OCT is compared conceptually to its close analog of Ultrasound where images are generated based on the time-of-flight acoustic reflections caused by changes tissue acoustic impedance. Since the speed of sound at 1.54m/msec in tissue is significantly slower than the speed of light in tissue 230,609m/msec, direct time of flight measurements cannot be made with conventional electronics. Therefore, OCT utilizes the principals of interference to gate the optical time-of-flight reflections from biological samples[2] compared to a reference reflection shown in Figure 1.

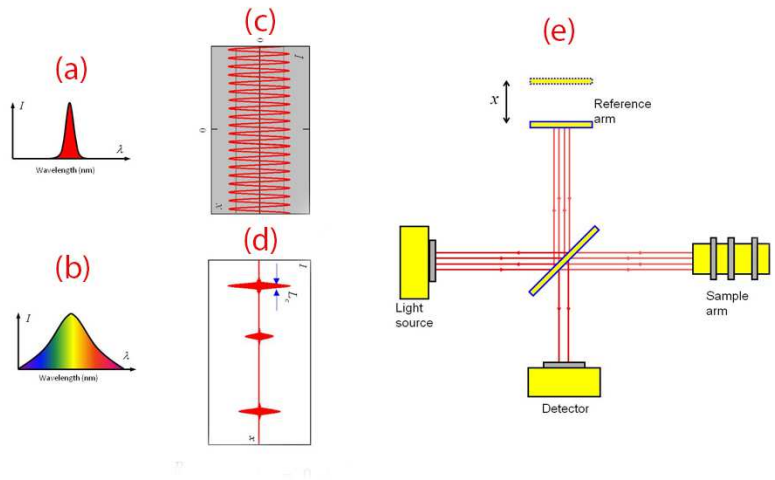

Figure 1 (a) Narrow bandwidth coherent laser source (b) wideband low-coherent laser source spectrum (c) interferogram resulting from the use of a narrow bandwidth coherent laser source not providing any information regarding the reflections along the traversed light path (d) interferogram resulting from the use of a wideband low-coherent laser source exhibiting coherent gating effect of reflections at different path length delays (e) schematic of a time domain optical coherence tomography system with a mobile reference arm. Depth resolved OCT signals are calculated as the reference mirror is moved from one reference arm x position to the next.

Contrast in OCT images is generated through the relationship between the wavelength of incident low-coherent light and the refractive index and size of biological scatters and absorbers. OCT imaging systems resolution can be broken into two parts: the depth resolved or axial resolution and the lateral resolution across each OCT image frame. Axial depth resolution is related to the coherence length of the low-coherent light source used (1-1)

$$L_c = \frac{2\ln 2}{\pi}\frac{\lambda^2}{n_s \Delta\lambda} = 0.44\frac{\lambda^2}{n_s \Delta\lambda} \qquad (1\text{-}1)$$

Where L_c the coherence length of the partially coherent laser light source is dependent on center wavelength λ and the full width half maximum laser bandwidth $\Delta\lambda$. The lateral or transverse resolution in OCT images is determined by the objective lens [3] used on the interferometer sample arm as seen in Figure 2.

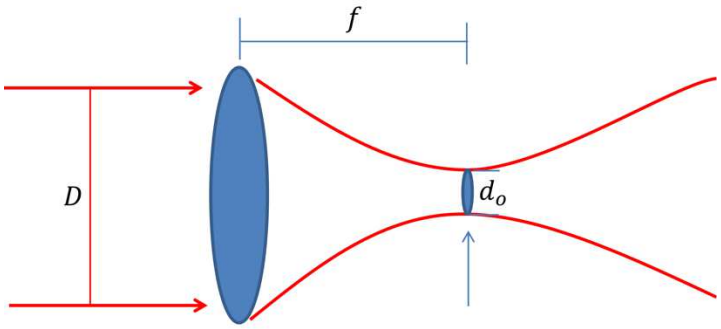

$$lateral\ resolution = d_o = \frac{2f\lambda}{D}$$

Figure 2 Schematic of sample arm objective lens illustrating the lateral resolution

Where λ is the center wavelength of the light source used and D is the input light diameter and f is the focal length of the objective lens. OCT imaging systems have evolved over the last 20 years to include a variety of different configurations that have increased the image acquisition speed, increased signal to noise (SNR) ratios and provided ultra-high resolution.

1.2.2 Spectral Domain Optical Coherence Tomography

SD-OCT is a subset of FD-OCT. SD-OCT are unique OCT systems that resolve the OCT interferogram using a spectrometer as can be seen in Figure 2. Following the laser source is an isolator to prevent damage to the laser cavity from back reflected light. The light is then incident on a beam splitter splitting light towards the reference and sample arms of the Michelson interferometer. The light reflected from the sample and reference mirror are re-combined at the beam splitter and reflected towards the spectrometer detection arm. The spectrometer then splits the interferometric signal based on wavelength spatially using a reflectance or transmission grating and is detected using a line scan CCD camera.

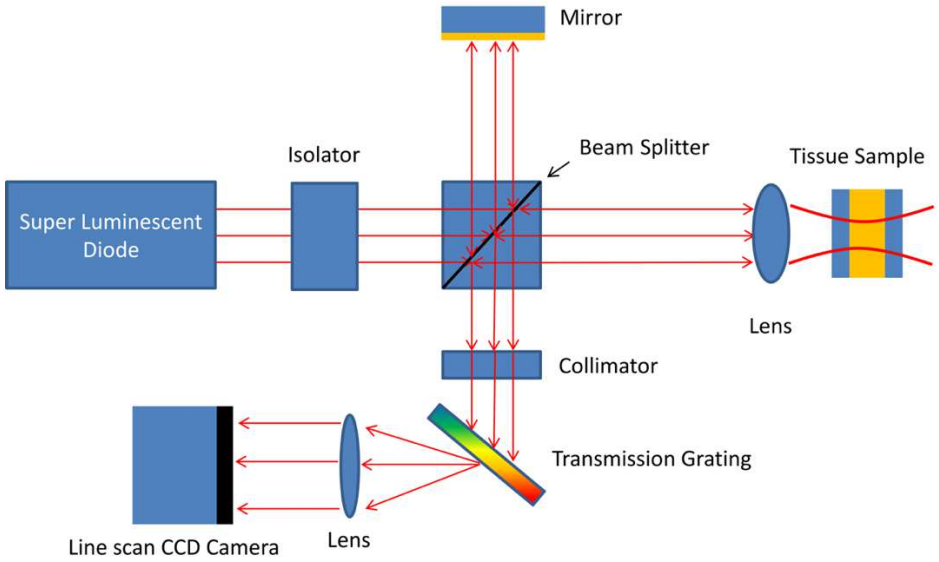

Figure 3 Optical schematic diagram of a free space spectral domain optical coherence tomography system. The input laser source shown is a partially coherent wideband super luminescent diode often utilized at 1310nm center wavelength with a 100nm bandwidth.

SD-OCT systems provide a greater internal phase stability between successive acquisitions of OCT interferograms(A-lines) due to the use of a solid-state laser. SD-OCT is limited in the signal to noise (SNR) roll off limited by a non-heterodyne detection configuration and use of a limited number of sampling pixels for the line-scan CCD (charge coupled device) camera[4]. To offset such short comings high speed tunable lasers with narrow instantaneous linewidths were created to allow for better SNR roll off while still maintaining the frequency domain aspect of OCT systems.

1.2.3 Swept Source Optical Coherence Tomography

Swept source optical coherence tomography (SS-OCT) is another method of frequency domain optical coherence tomography. In a SS-OCT imaging system a partially coherent high-speed (50kHz – 100kHz) near-infrared tunable laser is used in place of a wideband solid-state laser. At a given moment in time the swept laser outputs a narrowband spectrum with center wavelength k.

Physical pathlength differences are resolved in the frequency domain through a beating modulation envelope created by the interference of different frequencies in time

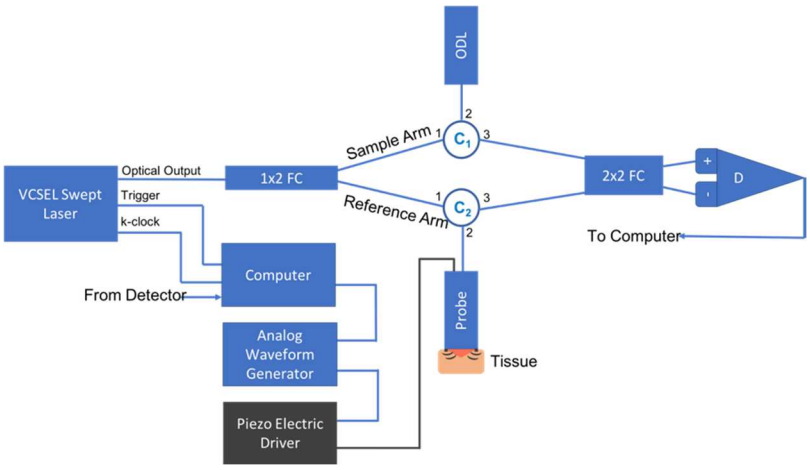

Figure 4 Swept source OCT system and piezo electric oral cancer imaging probe system schematic. The VCSEL swept laser in this schematic is 100kHz 1310nm center wavelength laser. An analog waveform generator provides the driving signal for the piezo electric element on the probe. This system setup is used for conducting optical coherence elastography of oral cancer.

Similarly, to an SD-OCT imaging system, a SS-OCT system also utilizes a Michelson interferometer optical setup with a static reference reflection and sample arm. The main difference between an SD-OCT and SS-OCT system is the detections scheme of the interferogram as can be seen in Figure 4. SS-OCT uses a heterodyne detection scheme with two single element photodiodes in a balanced detection configuration to cancel the common mode signal [4].

1.3 Overview of Dissertation

In my dissertation, I will be discussing the use of OCT as a diagnostic and monitoring tool to assess various medical conditions and diseases in-vitro and in-vivo. I will also discuss the modification of bench top OCT systems and probes to suite a more robust and user-friendly model for in-clinic and in-hospital use. The following is a summary of each chapter:

Chapter 1: Introduces the shortcomings in current medical imaging technologies and the diagnostic clinical unmet need. The chapter is then finished off with a brief outline of the various types of OCT imaging systems that have been developed and utilized in the later chapters.

Chapter 2: Discusses the use of OCT, scanning electron microscopy (SEM), fluorescence lifetime imaging (FLIM), and terahertz spectroscopy to study the structural and biochemical aspects of endotracheal tube bacterial biofilms as a pre-cursor for ventilator associated pneumonia. The aim of this chapter is to investigate the potential of using such imaging technologies to speed up the detection and differentiation of bacteria that can lead to the formation of ventilator associated pneumonia

Chapter 3: Regards the use of intensity-based OCT to assess the changes in the structure of the oral mucosa during the development of oral squamous cell carcinoma. A low-cost imaging system and probe developed for a pre-clinical efficacy trial will also be mentioned

Chapter 4: Will highlight the use of OCT in the field of dermatology to screen for changes in hair follicle and hair shaft cross-sectional area as a means of staging androgenic alopecia.

Chapter 2

Ventilator Associated Pneumonia Bacterial Biofilm Imaging

2.1 Endotracheal Tube In-situ Biofilm Imaging using Optical Coherence Tomography

2.1.1 Abstract

Biofilm formation has been linked to VAP, a prevalent infection in hospital intensive care units. Currently, there is no rapid diagnostic tool to assess the degree of biofilm formation or cellular biofilm composition. OCT is a minimally invasive, non-ionizing imaging modality that can be used to provide high resolution cross-sectional images. In this study biofilm deposited in critical care patients' endotracheal tubes were analyzed in-vitro. This study demonstrates the potential use of OCT as a diagnostic tool to asses and analyze the degree of biofilm formation and extent of airway obstruction caused by biofilm deposited on endotracheal tubes.

2.1.2 Motivation and Project Overview

Biofilm formation on the inner lumen of endotracheal tubes has been linked VAP, a prevalent infection in hospital intensive care units (ICUs) that results in an increase cost of hospital stay and increased morbimortality[5]. Biofilms initially form when microorganisms attach to a synthetic surface, multiply and develop an extracellular polymeric substance matrix that colonizes the growth of bacteria[6]. The presence of the endotracheal tubes in intubated patients increases the chances of contracting VAP due to a functionally compromised mucociliary system that would otherwise hamper formation of bacteria biofilm in the airway. It has been shown that these biofilms can be characterized by SEM in-vitro but require a sample drying and gold sputtering sample preparation process which can be a lengthy and arduous task and cannot be performed in-vivo[5]. OCT, a non-invasive, non-ionizing tomographic imaging technology can provide micrometer high

resolution cross-sectional images of various biological samples. It has been shown that OCT can be adapted to a rotational endoscopic probe-based system that can provide high resolution 3D volumetric information[7]. This body of work aim is to utilize optical coherence tomography as a tool to visualize biofilm formation at various time points in the biofilm lifespan. The eventual goal would be to image biofilm progression in-vivo and to correlate the progression of biofilm formation to nosocomial pneumonia in critical care patients.

2.1.3 Experimental Methods

OCT and SEM images acquired for three endotracheal tube samples collected from patients with the following intubation periods: sealed (un-opened), 24 hours post intubation, and 120 hours post intubation Fig 1-3. Extubated patient's endotracheal tubes were obtained from critical care patients at UCI Medical Center ICU and were transported in a sealed moist environment to the site of imaging. The tubes were then secured onto a sterile fabric chuck and imaged with a side-viewing helical scanning probe and OCT system previously described in[8]. Briefly, a 1310nm center

wavelength swept source with 50 kHz sweep rate and 100nm bandwidth laser source was used in a fiber-based Michelson interferometer.

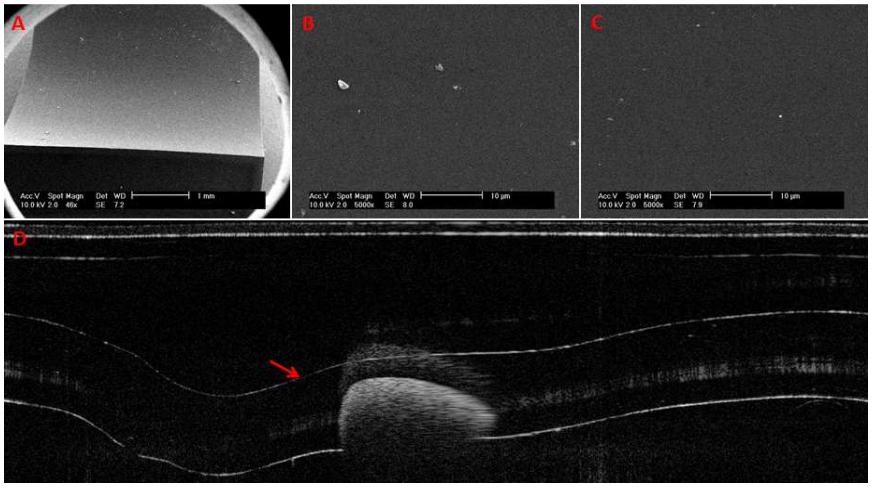

Figure 5 (a) 46x SEM image of sealed endotracheal tube segment (b) 5000x SEM image of same endotracheal tube showing (c) 5000x SEM of same endotracheal tube in different location (d) Corresponding OCT image arrow highlighting the lack of biofilm present on the inner lumen of the endotracheal tube.

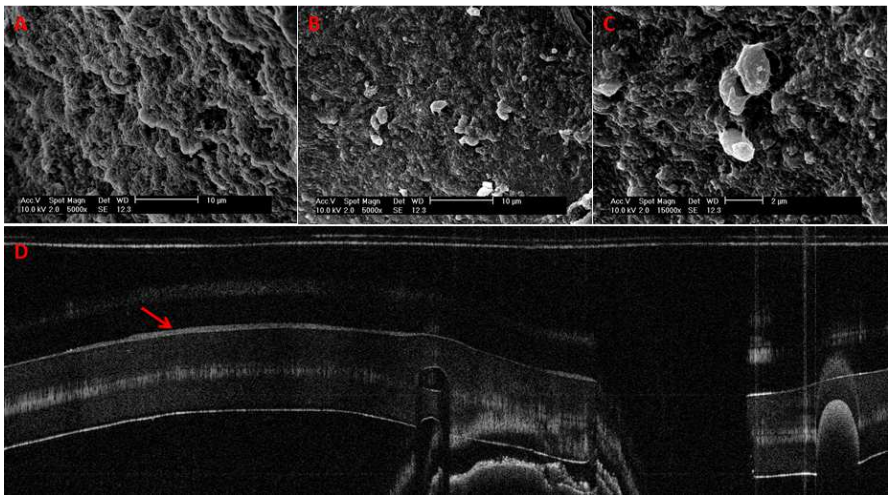

Figure 6 (a) 5000x SEM image of 24 hrs. post intubation endotracheal tube showing the presence of extracellular polymeric substrate (b) 5000x SEM image of same endotracheal tube in a different location (c) 15000x SEM of same endotracheal tube focusing in on cluster of cells(d) Corresponding OCT image red arrow highlighting the presence of biofilm on the inner lumen of the endotracheal tube

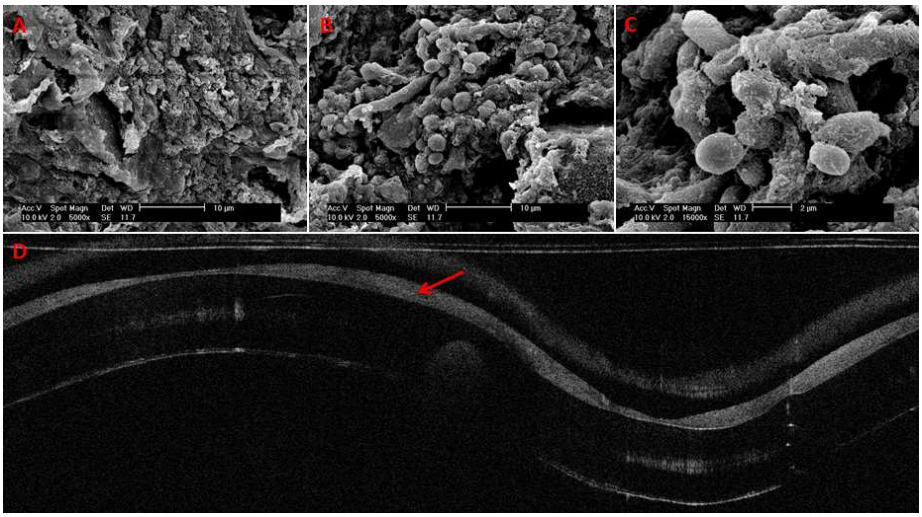

Figure 7 (a) 5000x SEM image of 120 hrs. post intubation endotracheal tube showing the presence of extracellular polymeric substrate (b) 5000x SEM image of same endotracheal tube in a different location (c) 15000x SEM of same endotracheal tube focusing in on a cluster of cells (d) Corresponding OCT image red arrow highlighting the presence of biofilm on the inner lumen of the endotracheal tube

The OCT system and probe had an axial resolution of 10μm in biofilm and a lateral resolution of 112μm. In addition, an acousto-optic modulator was used on the OCT system's reference arm to provide a carrier frequency of 150MHz for the OCT signal to take advantage of the full coherence length of the laser source. After OCT imaging, the samples were prepared for SEM using a standard dehydration and gold sputtering protocol. Endotracheal tubes were segmented using a surgical blade then fixed in formaldehyde and then changed to phosphate buffer for a short period of less than 24 hours pre-sample drying. Next samples were placed into 1% Osmium Tetroxide in double distilled water for 1 hour. Following Osmium tetroxide, the samples were placed in a varying concentration of Ethanol (EtOH 30%, 50%, 70%, 90%, and 100%) for 10 minutes at each concentration. Finally, each sample was placed into 4 mixtures of EtOH and Hexamethyldisilane (67%EtOH & 33% HMDS, 50% EtOH & 50% HMDS, 33% EtOH & 67% HMDS, 100% HMDS) for 15 minutes each. Samples were then gold sputtered (Cressington 308R, Ted Pella Inc.) to a thickness of 9nm. Scanning Electron Microscopy was then conducted on samples (Phillips XL-30

Field Emission ESEM) at 10,000 keV with variable levels of magnification namely 5,000, 10,000, and 15,000.

2.1.4 Results and Validation

Biofilm is present in both OCT and SEM images as seen in Figure 5-7. In OCT images Fig. 5-7(d) biofilm is indicated by a sharp increase in reflected OCT signal above the inner lumen of the endotracheal tube indicated by the red arrow as also indicated in[9]. In SEM images Fig. 5-7(a-c) the presence of biofilm can be seen through the presence of extracellular polymeric matrix encapsulating bacteria cell population. OCT and SEM images Fig. 5-7 for each sample established a correlation between OCT biofilm thickness indicated by the red arrows Fig. 5-7(d) and the complexity of the biofilm scaffold and bacteria colony present in SEM images can be observed Fig. 5-7 (a-c). It should be noted that the SEM data for the control sealed endotracheal tube Fig. 5 has some dust debris artifacts that could be mistaken for cells present. The average size of single bacteria and cellular population density was identified and measured in SEM images shown in Fig. 8 (Image J, National Institutes of Health). A mean cellular diameter of 1.34μm with a standard deviation of 0.463μm was measured and correlates well with previous bacteria characterization literature of bacteria commonly found in biofilms[10,11]. An increase in cellular density was observed through 5000x magnification SEM data between 1 and 5-day intubation endotracheal tubes. A 50% increase of bacterial cells was observed between 1 and 5-day intubated tube's cellular density population in a field of view of 46.84 x 35.13μm.

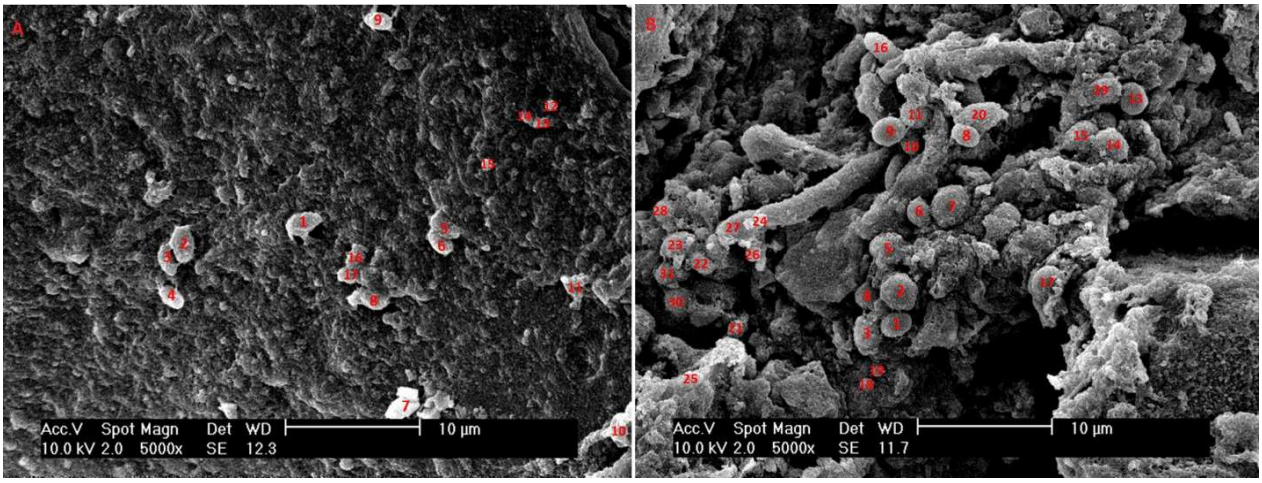

Figure 8 (a) SEM image of endotracheal tube extubated after a period of 1-day intubation. (b) SEM image of an endotracheal tube extubated after 5 days of intubation. Red numbering in both images indicates bacterial cells counted towards cellular density and average cell diameter.

Endotracheal tube airway obstruction was assessed utilizing the intensity-based OCT images and an imaging processing algorithm developed in MATLAB (MathWorks Natick, Massachusetts). The surface of the biofilm was manually identified and the number of pixels between the biofilm surface and the side viewing probe sheath were recorded Fig. 9. This process was conducted across sample sets of 40 and 80 OCT-B scans volumes that begin at the distal tip of the endotracheal tube with an axial spacing of 250µm between ET tube cross sections. A decrease of 21.47% of airway volume outside of the side viewing probe was observed between the 1 and 5-day intubation period endotracheal tubes for an OCT volume comprising of 40 OCT B-scans. When the OCT B-scan volume size increased by a factor of 2 to 80 OCT B-scans, an increase of only 3.42% to 24.88% obstruction was noted. This suggests that potentially one could use the area of most pronounced biofilm formation at the distal tip of the endotracheal to rapidly assess airway obstruction.

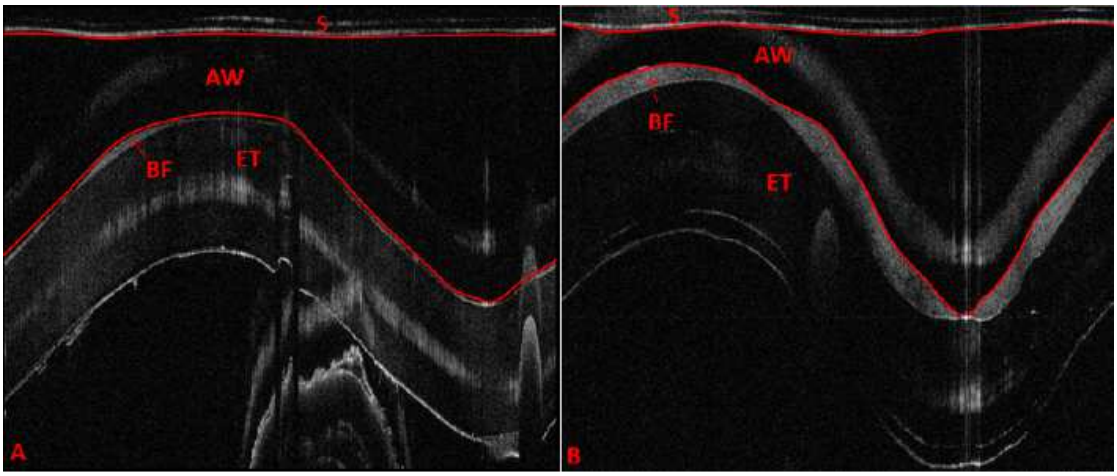

Figure 9 (S) probe sheath (BF) Biofilm (ET) Endotracheal tube (AW) airway between probe sheath and biofilm (a) OCT B-Scan of 1 day intubated endotracheal tube (b) OCT B-Scan of 5 day intubated endotracheal tube red lines in both images representing the boundary that was measured for airway obstruction calculation

2.1.5 Conclusion and Future Work

Through this study it has been shown that OCT could potentially be used as a tool to assess the extent of biofilm formation and airway obstruction. It has been shown that there exists a relationship between biofilm thickness detected at various intubation time points by comparing the thickness of the biofilm in OCT intensity-based images and the complexity and density of the biofilm structure observed in SEM. Using OCT intensity-based images we plan to analyze the thickness and structure of the biofilm at which intubated patients in the ICU contract VAP. Additionally, future work will be done to further analyze the biofilm subcomponents in terms of bacterial biomass as well as bacterial phenotype present and in what concentrations.

2.2 Fluorescence Lifetime Imaging of Bacteria

2.2.1 Fluorescence Background

Fluorescence lifetime imaging (FLIM) is a non-ionizing, minimally invasive imaging technique that provides in-vivo, high-resolution cross-sectional images with biochemical based contrast. FLIM is an extension of the traditional fluorescent microscopy that is utilized to understand complex multi-exponential decay biochemical fluorescent signals. It holds a unique advantage

over typical fluorescent microscopy due to its ability to resolve the intensity fluorescent signals independent of fluorophore concentrations. Furthermore, FLIM can provide detailed information with respect to fluorescent signals of biomolecules such as nicotinamide adenine dinucleotide (NADH), an indicator of cellular metabolism. Multiple fluorescent decay lifetimes are present for NADH based on the local chemistry and redox state surrounding NADH. It has been shown in the literature that the lifetime of NADH could be used to classify and differentiate bacterial phenotype[12]. To better understand the principle, Figure 10 shows a typical Jablonski diagram illustrating excitation and fluorescent emission.

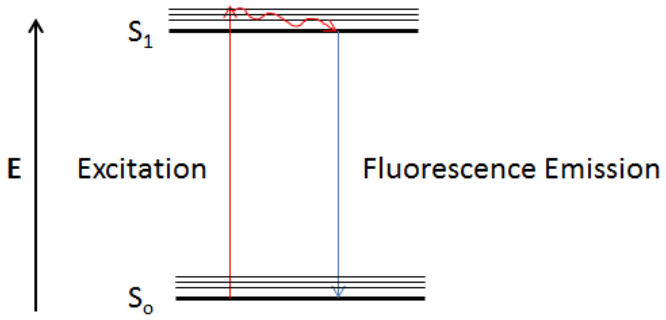

Figure 10 Jablonski diagram illustrating excitation and fluorescence emission

A molecule is excited from the ground state (S_o) by an input of energy in the form of laser light to an excited state S_1. The electrons in the excited state will then spontaneous fall back down to the ground state and emit a photon of light that is captured and analyzed as fluorescence (2-1).

$$I(t) = I_o e^{-\frac{t}{\tau}} \qquad (2\text{-}1)$$

Where $I(t)$ is the fluorescent intensity at time t, I_o the fluorescent intensity at time t = 0, and τ that represents the fluorescence lifetime decay constant. In this instance the intensity of the fluorescent signal is dependent on the amount of the fluorophore present and insensitive to measuring the potentially complex fluorescent lifetime component of the exponential decay that could be multi exponential. Frequency Domain FLIM (FD-FLIM) on the other hand is

insensitive of fluorophore concentration and can accurately determine a multi exponential fluorescent decay process.

FD-FLIM, like two photon fluorescence microscopy uses a tunable pulsed Ti: Sapphire laser, but instead of capturing the bulk fluorescent signal the modulations in laser intensity as well as phase between excitation and emission are analyzed. The amplitude and phase modulation can then be related to the fluorophores lifetime via (2-2)**.**

$$\tau_\varphi = \left(\frac{1}{\omega}\right)\tan(\varphi)\ , \tau_m = \left(\frac{1}{\omega}\right)\left(\frac{1}{m^2}-1\right)^{\frac{1}{2}} \tag{2-2}$$

Where τ_φ and τ_m are the phase and modulation lifetimes respectively, ω is the angular frequency of the excitation source, m is the modulation of amplitude between excitation and emission, and φ is the phase difference between excitation and emission. To better visualize complex mutli-exponential fluorescent lifetime decays, phase and amplitude information can be converted to the phasor space for a clear spatial visualization of pure and mixed lifetime populations such as bound and unbound NADH[13]. Where $g_{i,j}(\omega)$ and $s_{i,j}(\omega)$ are the representative phasor vector coordinates at the excitation laser's angular frequency ω of the i,j pixel in a 2D fluorescence signal, $m_{i,j}$ is the signal amplitude modulation between emission and excitation, and $\varphi_{i,j}$ is the phase modulation of the emission with respect to the excitation(2-3).

$$g_{i,j}(\omega) = m_{i,j}\cos\left(\varphi_{\mathrm{i,j}}\right), s_{i,j}(\omega) = m_{i,j}\sin(\varphi_{i,j}) \tag{2-3}$$

2.2.2 Experiment: FLIM of Endotracheal Tube Biofilm

Endotracheal tubes were transferred from the UCI Medical Center (Orange, CA) to the Laboratory for Fluorescence Dynamic at the University of California, Irvine, for FLIM imaging. Biofilm mucus samples were mechanically removed from the inner lumen of

extubated endotracheal tubes using a plastic scrapper and smeared across a quartz coverslip. A clear piece of quartz glass placed on top sealed the mucus bacterial sample completing sample preparation for a two-photon fluorescence microscope. Frequency-domain fluorescence life time images were acquired using deep tissue fluorescence imaging system utilizing a tunable Ti: Sapphire pulsed laser [14]. An area of 72µm x 72µm was imaged with an average pixel dwell time of 32µs for a 256x 256 pixel area. Phasor fluorescence life time plots as can be seen in Figure 11 were generated for the bacterial biofilm sample. From the false colored FLIM phasor we see a clear distribution of fluorescence lifetime around the bound NADH.

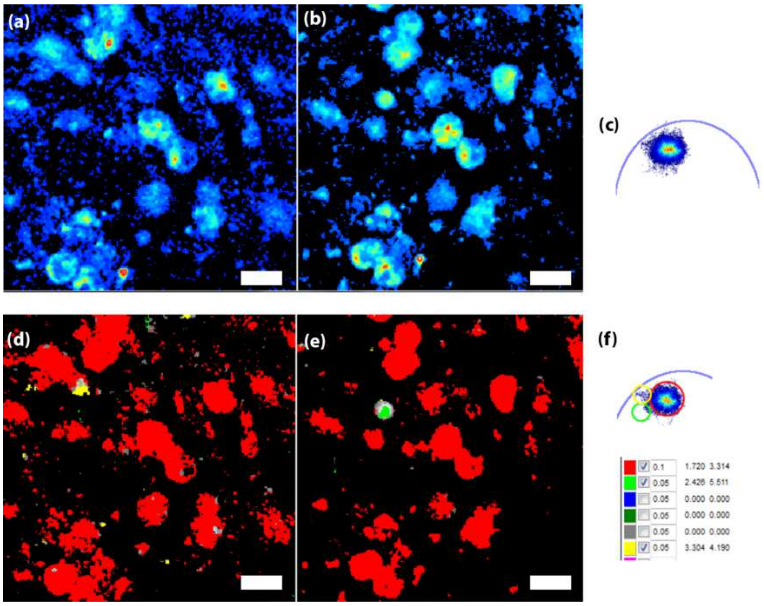

Figure 11 Fluorescence lifetime images and representative phasor plots of bacterial biofilm mucus secretions. (a)(b) False color fluorescence lifetime images and corresponding color-coded phasor plot (c). Scale bars indicate 10µm (d)(e) Grouped phasor representation of the previous biofilm mucus FLIM images shown in the phasor plot (f). Phasor plot with false color FLIM phasor grouping. Phase and modulation values and corresponding color grouping are shown below the phasor plot.

2.2.3 Results and Discussion

From Figure 11, one can see that the biofilm mucus secretions exhibit a uniform distribution of bound NADH fluorescence lifetime across the sample. There appears to be specific internal regions of select larger cell like components of the sample that have specific concentrations of bound NADH. These areas could represent the mitochondria of the cell's that are actively consuming ATP producing NADH and FAD in the Krebs cycle. Taking note of cell size, one could say that this biofilm mucus sample contains a mixture of bacteria and mammalian cells. This work suggests that bacterial biofilm secretions on the inner lumen of endotracheal tubes are fluorescent and that further work would need to be completed to fully characterize the composition of the biofilm mucus secretions.

2.2.4 Experiment: FLIM Lifetime Signature of Bacterial Clinical Isolates

Cystic fibrosis patient's bacterial clinical isolates were utilized in a proof of concept experiment that tested the hypothesis that bacteria could be separated out in FLIM phasor space. Pseudomonas aeruginosa (P1), Rothia mucilaginosa, Streptococcus salivarius, Stenotrophomonas maltophilia, were thawed from a frozen glycerol stalk and plated in Todd Hewitt agar. The agar plates were incubated for 24 hours at 37 degrees C with 5% CO_2. Two visible colonies were scrapped of the agar with a sterile loop and re-suspended in 20ml of Todd Hewitt broth. These samples were then placed on a shaker in a room at 37-degree C for 24 hours. The cultures present in the 20ml culture were no presumed to be fully differentiated stationary bacterial phenotype with minimally genetic variation beyond the point of further replications. 1 μL aliquots of the 20ml solution for each bacteria type were plated as duplicates in an 8 well plate quartz microscope slide. Two-photon FD-

FLIM using an 800nm 80MHz Ti: sapphire pulsed laser was conducted across the duplicate samples for the 4 bacterial strains previously mentioned.

2.2.5 Results and Discussion

Fluorescence lifetime phasor plots were generated for NADH and FAD emission spectra as seen in Figure 12.

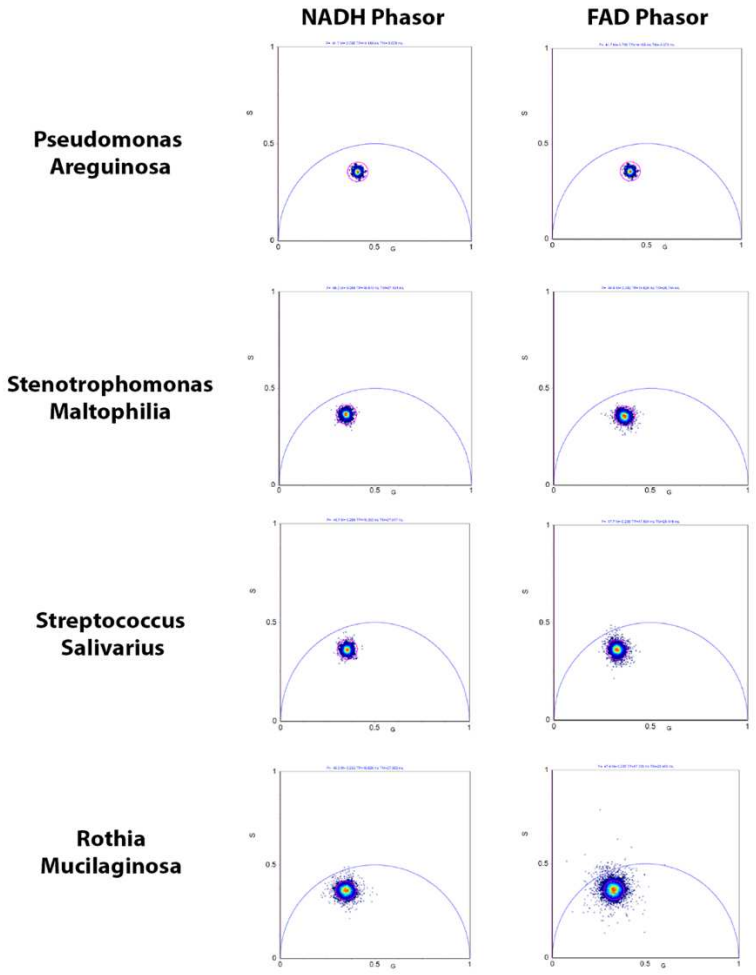

Figure 12 FLIM phasor plots for the NADH and FAD emission for the four clinical isolates.

Variables namely, s-average, g-average, phase and modulation of the FLIM phasor signal were analyzed for their classification power amongst the four clinical isolates. The four variables were assessed in duplicates across both NADH and FAD channels as can be seen in Figure 13.

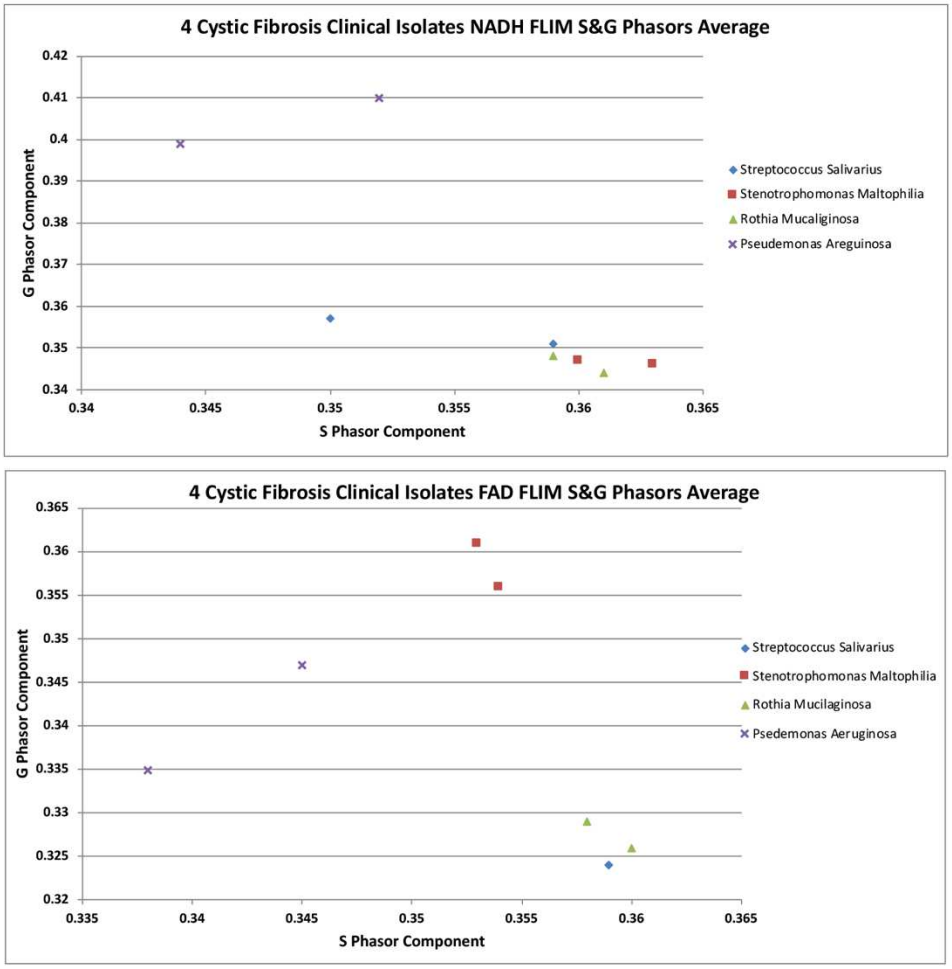

Figure 13 S and G NADH and FAD FLIM phasor components for four cystic fibrosis clinical isolates

Classification of the four bacteria was also assessed through the ratio of modulation and phase of NADH and FAD channels (2-4,2-5) as can be seen in Figure 14.

$$M_{ratio} = \frac{M_{NADH}}{M_{FAD}} \tag{2-4}$$

$$P_{ratio} = \frac{P_{NADH}}{P_{FAD}} \tag{2-5}$$

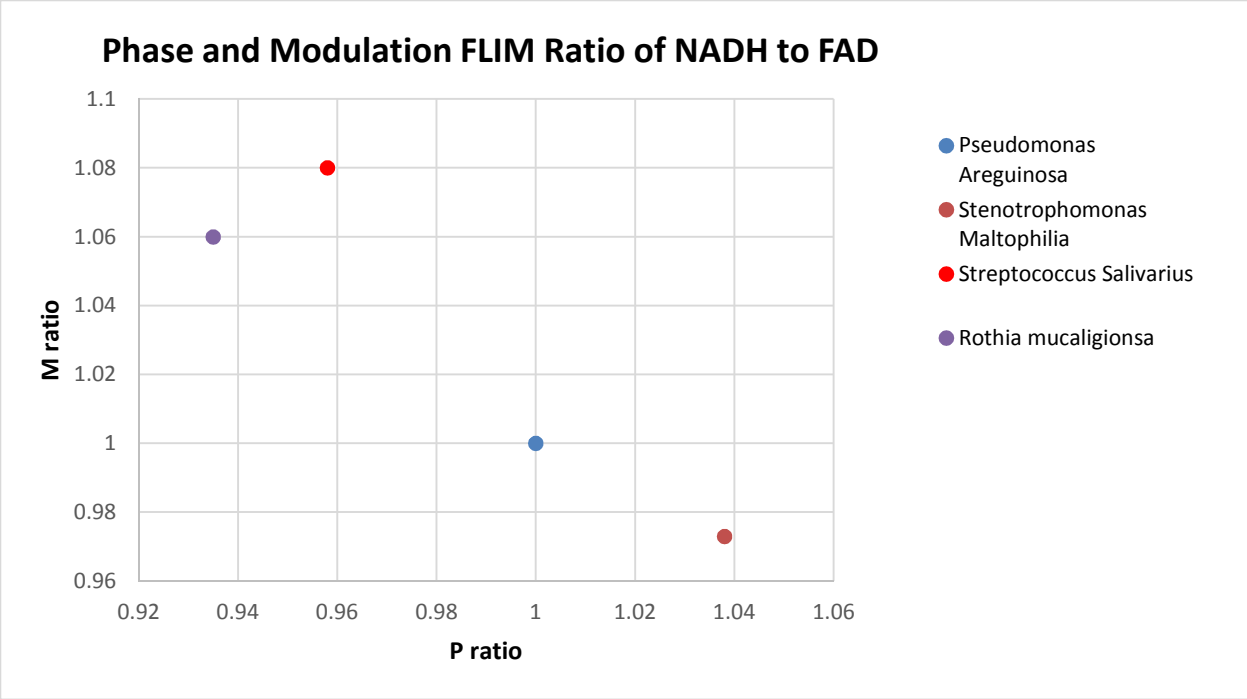

Figure 14 Ratio of NADH to FAD FLIM Phase and Modulation of the four cystic fibrosis clinical isolates.

The separation between the four clinical isolates in the phase and modulation could be appreciated by varying values for the s and g average FLIM phasor values respectively for NADH and FAD channels. NADH s and g average values show separations between Pseudomonas Aeruginosa, Streptococcus Salivarius compared to Rothia Mucaliginosa and Stenotrophomonas Maltophilia. FAD s and g average values show greater classification power between Pseudomonas Aeruginosa and Stenotrophomonas Maltophilia from Rothia Mucaliginosa and Streptococcus Salivarius. Lastly the phase and modulation lifetime ratio of NADH and FAD showed separation between two groups of bacteria namely Rothia Mucaliginosa, Streptococcus Salivarius and Pseudomonas Aeruginosa, Stenotrophomonas Maltophilia. Through these experiments we have found that it would be most challenging to differentiate between Rothia Mucaliginosa and Streptococcus

Salivarius given these parameters. The varations observed in the FLIM phasor data could be explained by the varying in phenotype enzymatic chemistry that would alter NADH and FAD lifetime characteristics. Although this experiment has only duplicates for each observational measurement, the results discussed herein provide reasonable preliminary data and proof that cystic fibrosis bacterial isolates can be differentiated utilizing their NADH and FAD FLIM lifetime data. Future studies will need to be completed to elucidate the complete mechanism supporting the variability in biochemistry allowing for such observations.

2.3 Terahertz Spectroscopy

2.3.1 Terahertz Motivation

Terahertz spectroscopy utilizes electromagnetic radiation in the far infrared (IR) from 0.1 to 10 THz corresponding to 30 to 3000μm. Wavelengths in the far IR terahertz regime are understood to excite low-frequency vibrational modes such as the weak interactions including hydrogen bonds, van der waal forces, and non-bonding hydrophobic interactions[15]. Due to these unique characteristic biochemical interactions THz radiation holds potential as a spectroscopic means of bacterial detection. The contrast in THz spectra between bacteria phenotype can be understood by the differing metabolite expressions, cellular components composition expressed in each unique strain[16]. Terahertz spectroscopy also has the potential of assessing bacterial viability through the water absorption sensitivity in the far IR[17].

2.3.2 Time Domain Terahertz Spectroscopy (TD-THz)

Time-domain terahertz spectroscopy systems can be realized as a pump-probe system and in a photomixing spectrometer design. Pump-probe TD-THz, as can be seen in Figure 11a typically utilize a femtosecond laser operating at 100-MHz repetition rate to produce 100-fs laser pulses[18].

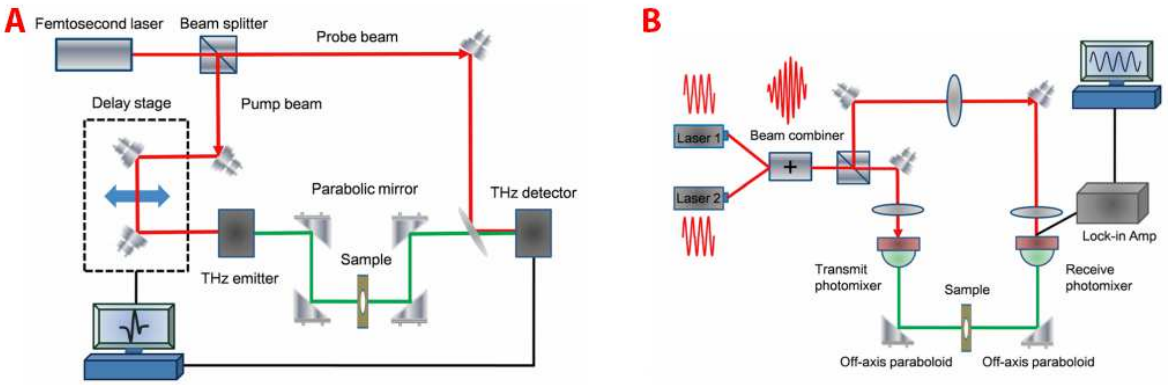

Figure 15 (A) Pump probe terahertz system schematic that utilizes a femtosecond pulsed laser as a means of terahertz wave generation (B) Photomixing terahertz system schematic that utilizes two lasers with an frequency offset to create a terahertz beat frequency.

The femtosecond laser is initially split into a pump beam utilized to generate terahertz waves and probe beam to coherently gate the detecting terahertz element. Using a pump probe-based system the phase and amplitude of the THz electrical field can be resolved. Other methods such as photomixing terahertz spectroscopy, as seen in Figure11b can be utilized to obtain high spectral resolution terahertz transmission spectrums. Through the careful selection of diode center frequency and the difference between the two lasers a terahertz beat frequency will be generated. By slowly tuning the wavelength of the frequency separated diode variable terahertz wave will be generated.

2.3.3 Experimental Design

Four cystic fibrosis clinical isolates namely: Pseudomonas aeruginosa (P1), Rothia mucilaginosa, Streptococcus salivarius, Stenotrophomonas maltophilia, were thawed from a frozen glycerol

solution and plated in Todd Hewitt agar. The agar plates were incubated for 24 hours at 37 degrees C with 5% CO_2. Approximately 26mg of bacterial biofilm colonies of each strain were scrapped off their respective agar plates into Teflon single well plates with a sterile loop. A piece of filter paper was then placed over the bacterial biofilm matrix and pressed down into the Teflon well to create a flat specimen for minimal distortion of the terahertz incidence radiation as can be seen in Figure 15.

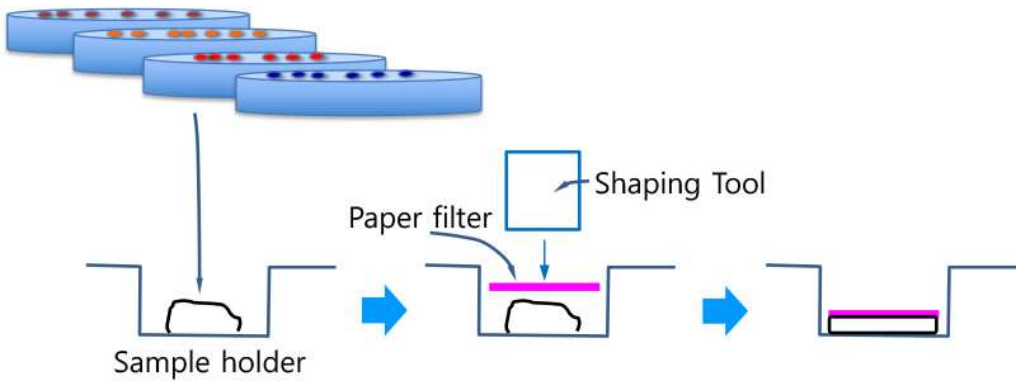

Figure 16 Example workflow of how to prepare samples for terahertz imaging.

Prior to terahertz spectroscopy a visible light image of each sample was taken with a visible light microscope and cell phone. Each sample was spectroscopically analyzed at three time points post plating: immediately after plating, 6 and 12 minutes after plating. The terahertz absorption spectrum was acquired from 300Ghz to 1 THz at a 25GHz step size. A custom LABVIEW VI controlled the onboard wavelength tuning of the varying frequency diode and lock-in-amplifier. The sample arm was comprised of a 5 mm collimated beam in transmission mode that irradiated the samples resting on a Teflon plastic well. Background Teflon terahertz spectrums were acquired for background subtraction. Total terahertz spectrum acquisition time was 6 minutes for each specimen. Terahertz spectra of plated bacterial biofilm colonies was measured immediately after

plating and at 6-minute intervals up till 12 minutes after plating. After terahertz spectroscopy samples were imaged using a swept source vertical cavity surface emitting laser optical coherence tomography (SS-VCSEL-OCT) system. The thickness of bacterial samples was resolved with a commercial VCSEL system (VEGA) from Thorlabs. The laser has a center wavelength of 1310nm with an A-line sweep rate of 200KHz. A fiber-based Michelson interferometer was used with a two-axis galvanometer microscope scanning probe. Bacterial samples were scanned in a 5 x 5 mm area providing adequate coverage of the plated bacterial biofilm. Axial and lateral resolution of the imaging system were 9μm and 15μm respectively. From the OCT tomographic data sample thickness was measured and provided for the calculation of the terahertz extinction coefficient[15] calculated by (2-6, 2-7, 2-8).

$$n(f) = \frac{|\phi_s(f) - \phi_{ref}(f)| * c}{2\pi f d} + 1 \tag{2-6}$$

$$k(f) = ln\left[\frac{4n(f)}{p(f)[n(f)+1]^2}\right]\frac{c}{2\pi f d} \tag{2-7}$$

$$\alpha(f) = \frac{4\pi f k(f)}{c} \tag{2-8}$$

Where n(f) the refractive index as a function of frequency is equal to the difference in $\phi_s(f)$ and $\phi_{ref}(f)$ phase angles of the power and transmission of sample and reference respectively, c speed of light, f frequency, and d optical path. The extinction coefficient k(f) is dependent upon previously described parameters and the amplitude ratio of sample and reference p(f).

2.3.4 Experimental Results and Discussion

Terahertz spectrum for the 4 cystic fibrosis bacteria can be seen in Figure 16. One can see a stark difference between the original sample absorption and the absorption after 12 minutes post exposure to atmosphere. This can be explained by biofilm construct dehydration from the biofilm

from exposure to filter paper and the atmosphere seen in Figure 17. These findings are confirmed with OCT images illustrating filter paper bacterial cultures that have dried up off the Teflon surface. The 500 to 900GHz spectrum of terahertz radiation is known to be sensitive to water absorption that would also be reflected in the temporal decrease in overall terahertz absorption. Although there is no clear distinction between bacterial strains based on their transmission terahertz absorption spectra, their absorption coefficient provided classifying power. The absorption coefficient provided a clear means of separating P1, SM, and RM as can be seen in Figure 18. The absorption coefficient for SS provided mixed regions of clearly distinguishable values when compared to the rest. calculated based on the sample thickness observed in OCT based tomograms as can be seen in Figure 12B. SS could have provided a variable terahertz absorption profile due to inconsistencies with results could be a result of

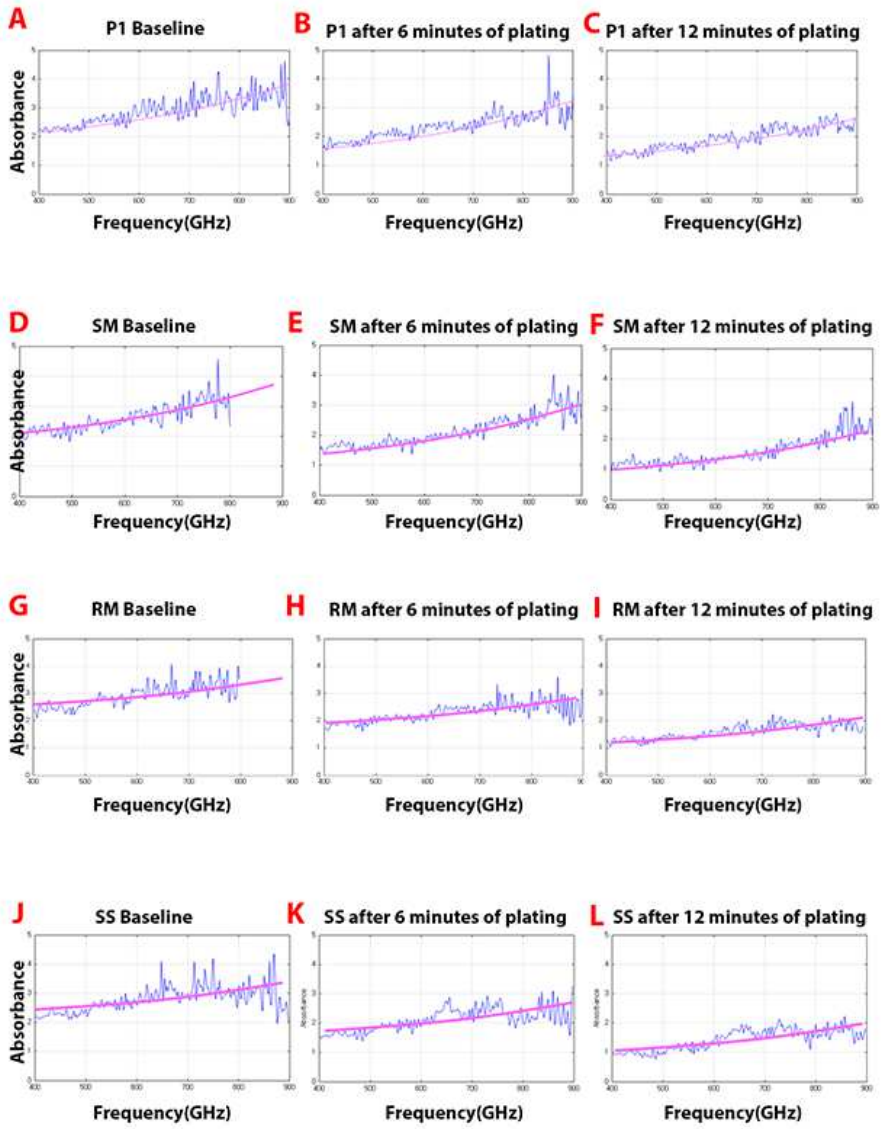

Figure 17 Sequentially acquired terahertz absorption spectrums taken at 6 min intervals post plating for (A-C) pseudomonas aeruginosa, stenotrophomonas maltophilia (SM), rothia mucilaginosa (RM), and streptococcus salivarius (SS).

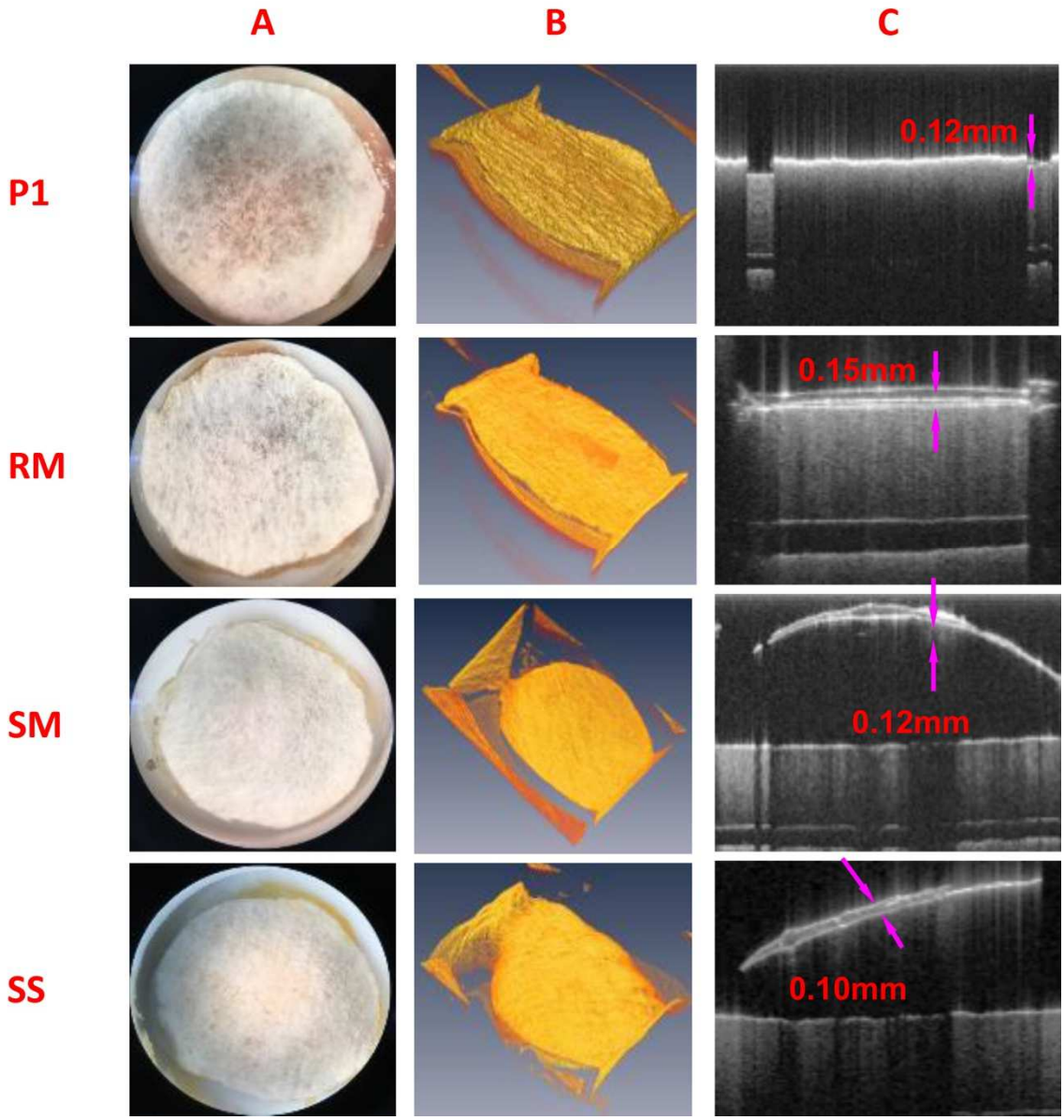

Figure 18 (A) Visible light images of the respective clinical isolate plated in a Teflon well with filter paper pressed on top (B) 3D-OCT reconstructions (C) 2D OCT B-scans of the four clinical isolates.

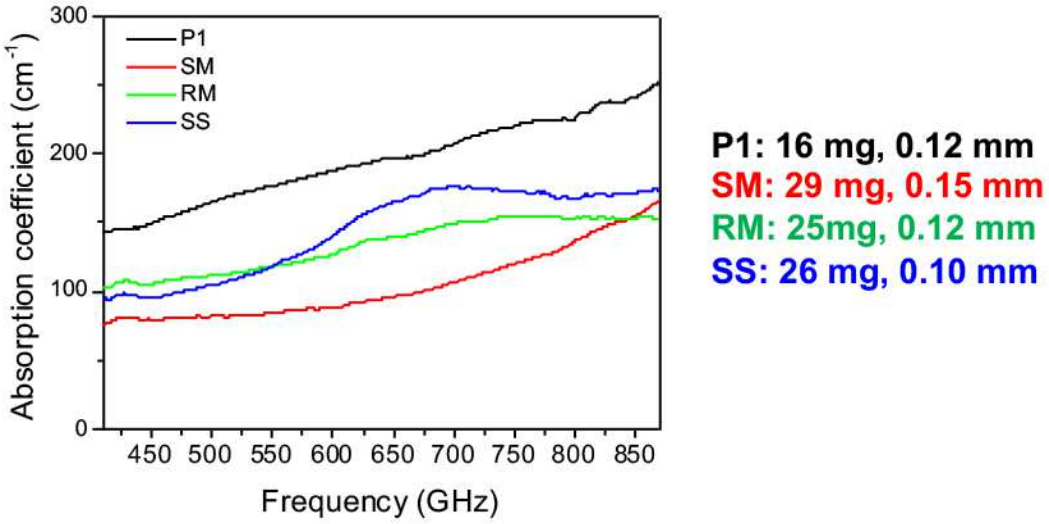

Figure 19 Combined terahertz absorption coefficient frequency spectrum for four clinical isolates namely pseudomonas aeruginosa (P1), stenotrophomonas maltophilia (SM), rothia mucilaginosa (RM), streptococcus salvarius (SS).

2.3.5 Conclusion and Future Work

Terahertz spectroscopy has been conducted across 4 cystic fibrosis clinical isolates using a photomixing time domain terahertz spectroscopy system. Terahertz spectroscopy was demonstrated as a means of rapidly finger printing and identifying bacterial phenotype through their relative water absorption and presence of unique protein metabolites. Further experiments will need to be conducted to assess the feasibility of phenotypically resolving mixed populations of bacteria.

2.4 Chapter Summary

Three unique imaging modalities namely OCT, FLIM and Terahertz spectroscopy have demonstrated the ability to identify macroscopic structure of the biofilm matrix as well as its biological constituents. These results should be a stepping stone proof of principal body of work

requiring further investigation to fully characterize the biochemical and physiological trends observed.

Chapter 3

Optical Coherence Tomography as a Screening and Diagnostic Adjunct for Oral Cancer

3.1 Novel Optical Coherence Tomography Probe for Oral Cancer Screening and Triage in a Low Resource Setting

3.2 Abstract

Oral cancer is the sixth most common cancer worldwide, predominantly seen in low and middle-income countries. Two thirds of all cases are detected at a late stage when prognosis and treatment outcomes are poor. Oral lesions are commonly detected by visual inspection, followed by surgical biopsy and histopathological analysis. This process is invasive, resource intensive, and poorly suited to screening remote or underserved at risk populations. Prior studies suggest that Optical Coherence Tomography (OCT), a minimally invasive tomographic imaging technology, can be used to identify premalignant or malignant change in the oral mucosa. In this study, a novel mobile OCT imaging system was designed, constructed and tested for its performance as a point-of-care oral diagnostic device. Its performance in low-resource locations was assessed in Bangalore, India. Twenty patients with suspicious leukoplakic or erythroplakia oral lesions and 10 healthy subjects were enrolled in this first pilot study. Two dimensional OCT images as well as clinical examination data, risk habit history and histopathology were collected. Retrospective data from 10 subjects each with typical OCT images for oral mucosal health, dysplasia and malignancy were evaluated in a blinded fashion by visual scoring and image processing techniques. It

was found that the OCT image processing algorithm preformed at and in certain cases exceed the performance of visual observer scoring of OCT images.

3.3 Introduction

Oral squamous cell carcinoma (OSCC) ranks as the sixth most common cancer worldwide, accounting for approximately 400,000 new cancer cases annually[19]. Two-thirds of OSCC cases originate in low-resource countries of the world[20]. The high morbidity and mortality of OSCC are attributed primarily to late diagnosis, with more than two thirds of OSCC cases diagnosed at loco-regionally advanced states [21]. Prognosis of OSCC is stage dependent, with an average five-year disease-free survival rate of 80-90% if diagnosed at stage I and II and only 20% if diagnosed at stage III and IV [19]. Thus, early detection and prompt treatment offer the greatest hope to patients with oral cancer, providing the best chance of minimally invasive treatment and better disease outcomes.

Oral cancer is frequently preceded by oral potentially malignant lesions (OPML) which typically present as red, white or speckled lesions seen in Figure 19. Although 1.5%-20 % of these lesions progress to OSCC over 5 years[22,23], malignant transformation rates may be as high as 51% for individual lesions such as erythroplakia[23]. The mechanism of malignant transformation remains unclear, and there are no clear prognostic markers informing on risk in individual patients or to guide the specialist's treatment plan [24]. Therefore, patients with OPMLs require frequent and careful monitoring to ensure early detection of malignant transformation. Currently, monitoring is performed by visual examination and incisional/excisional biopsy. The diagnostic accuracy of visual examination is unreliable, and biopsies have poor patient compliance, requiring specialist skills as well as laboratory

facilities that are typically limited to high-resource environments and can be expensive[22]. The key challenge to reducing the mortality and morbidity of OSCC is to generate strategies to identify and detect OSCC at an early stage, and to develop a non-surgical means of monitoring lesions that are at risk of malignant transformation. By overcoming this barrier OSCC outcomes will improve considerably. In low and middle-income countries (LMICs) this need is particularly urgent in remote areas due to the very limited availability of oral cancer specialists.

Approximately two-thirds of OSCCs occur in low- and middle-income countries (LMICs), with very high rates in South and South-East Asia (e.g., in Bangladesh, India, Malaysia, Nepal, Pakistan, Sri Lanka, Thailand, and Vietnam) [24]. Tobacco smoking and chewing, betel quid use, alcohol abuse and poor oral hygiene are the primary factors for greater oral cancer prevalence[25]. India has the 8th highest age-adjusted death rate of head and neck cancers in the world, and among females the rate is the highest in the world[26,2728]. The Indian sub-continent accounts for one-third of the world burden[29]. Oral cancer is the most common cancer in India, accounting for 40% of all cancers overall, and for more than 50% of all cancers in some areas of the country[29]. While the 5-year survival rate in the U.S. for OSCC is 62%, the survival rates is only 10-40% and cure rates around 30% in the developing world[30].

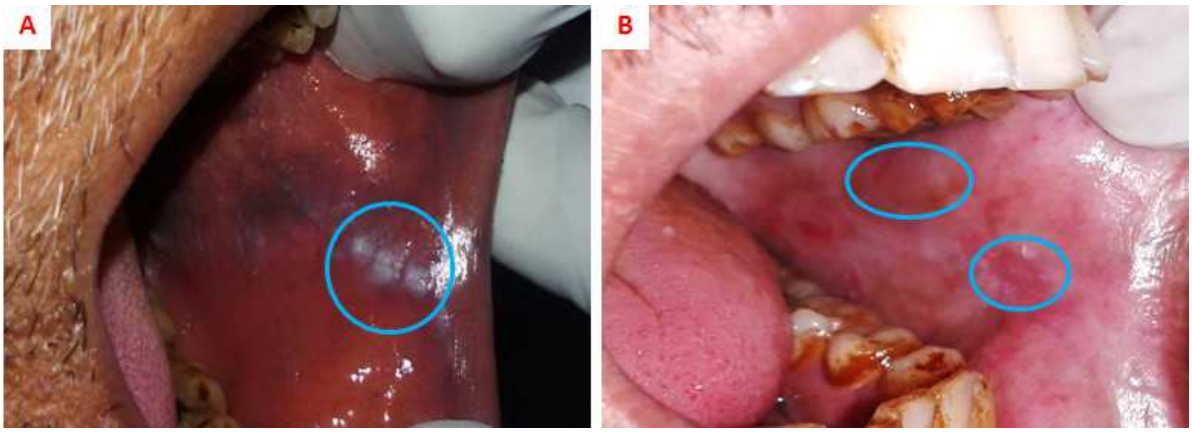

Figure 20 (A) Left buccal mucosa leukoplakia circled in blue (B) Left buccal mucosa erythroplakia circled in blue

Optical coherence tomography (OCT), a minimally invasive, non-ionizing imaging modality, can generate high-resolution cross-sectional images of near-surface abnormalities in complex tissues[31]. It can be compared to ultrasound imaging conceptually. Ultrasound generates tomographic images through resolving the time-of-flight acoustic reflections caused by differences in acoustic impedance of tissue anatomy. Given the relatively slow speed of sound in air and tissue, 330m/s to 1,540m/s respectively, conventional electronic analog to digital circuitry can be used to calculate the delay and intensity between the emitted ultrasonic waves and the reflected echo from the tissue sample[32]. Similarly, OCT can provide tomographic images through resolving the ballistic back scattered light-based echoes generated by differences in tissue refractive indices. Since the speed of light through air and tissue is several hundred thousand orders of magnitude larger than sound at 299,700km/s and 222,000km/s respectively, alternative approaches such as low coherent interferometry must be used to resolve light based echos[2]. Light from a low-coherent light source is utilized in a Michelson based interferometer comprising of a static reference reflection, probe-based sample arm, and balanced detection. Low-coherent light is initially

split into a reference and sample beam where their reflections are later combined, interfered, and detected. The difference in the distance traveled between the two interference arms will cause shifts in frequency that are captured in the interference fringe pattern. From the relationship between frequency and light physical traveled distance, the interference fringe pattern is converted into cross-sectional tomographic images of tissue generated at near histologic resolution with >5 μm depth resolution. The images show the macroscopic characteristics of the epithelial and sub epithelial structures. With an oral mucosal penetration depth of approximately 2mm, the imaging range of our OCT technology is suitable for interrogating the thin (0.2-1mm) human oral mucosa. Previous studies using OCT have demonstrated the ability to evaluate macroscopic characteristics of epithelial, sub epithelial, and basement membrane structures and show the potential for near histopathological-level resolution and close correlation with histologic appearance[33]. Long-term goal of this project is to develop an OCT-based diagnostic tool with immediate triage output for diagnosing OPMLs and OSCC. The aim of this first study was to design and construct a novel low-cost OCT imaging system with diagnostic algorithm, collect baseline normative data for oral tissues that were healthy, dysplastic or malignant, and assess its diagnostic accuracy in a low-cost setting.

3.4 Methods

This prospective clinical research was initiated after obtaining IRB Approval from The Narayana Health Medical Ethnics committee (NHH/MEC-CL-2015-279). Patients referred to

the Mazumdar Shaw Cancer Center, Bangalore, India, and clinically diagnosed to have OPMLs and malignant lesions were enrolled in the study. Patient overview is shown in Table 1.

Table 1 Study patient population description

Variables	Frequencies (n=30)	Percentages
Sex		
Male	17	57
Female	13	43
Age		
>40	16	53
<40	14	47
Risk Habits		
None	10	33
Tobacco	20	67
Drinking	0	0
Normal	10	33
Mild dysplasia	5	18
Moderate dysplasia	3	10
Severe dysplasia	2	6
OSCC	10	33

After a conventional clinical exam, the following six areas were imaged: left and right buccal mucosa, dorsal and lateral surfaces of tongue, labial mucosa, and floor of mouth mucosa. Additionally, any sites of leukoplakia and erythroplakia were imaged. Two to three averaged 1-D OCT B-scans 500 A-lines in length were acquired at each site shown in Figure 20c-h. Punch biopsies were then collected as per standard of care from any areas that appeared clinically suspicious and were subsequently processed for histopathological examination. The OPML and malignant lesions were reported as non-dysplastic, mild, moderate or severe dysplasia, or invasive carcinoma based on the World Health Organization criteria.

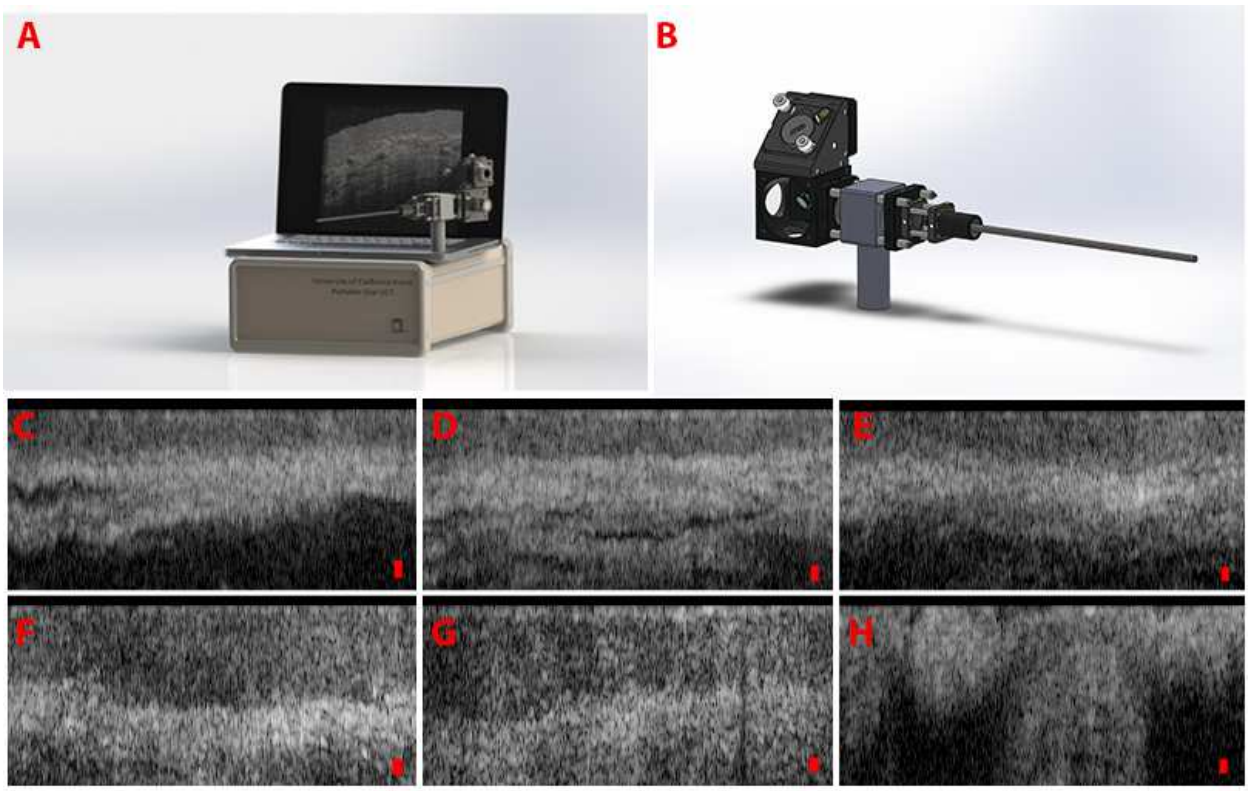

Figure 21 (A)Portable low cost optical coherence tomography system and probe (B) Close up isometric view of the 1D forward viewing OCT probe. 2D OCT B-Scans of various area acquired with such probe of the oral cavity including: (C) floor of the mouth (D) labial mucosa

In-vivo OCT images were acquired using an SD-OCT system and prototype 1-D scanning long GRIN rod probe Figure 20a,b. The SD-OCT system Figure 20a using center wavelength of 930nm has an axial resolution of 7.0µm and lateral resolution of 15.0 µm in air. Using a 20kHz 1024-point CCD line-scan camera on the spectrometer detection arm, an imaging speed of 1.2kHz was achieved. The 1-D long GRIN rod (Gradient lens corporation, Tremont NY) probe Figure 20b is comprised of a galvanic scanning mirror, a pair of scan lenses, a rigid one pitch gradient refractive index (GRIN) rod and an objective lens. A long rigid one pitch GRIN rod was used in this study to relay light from the proximal portion of the probe to the patient's tissue. For this study, the GRIN rod on the probe was designed to be longer to provide approximately 2ft of separation between the clinician and the patient to ensure

social gender appropriateness for a rural population in India. Retrospective data from 10 subjects each with typical OCT images for oral mucosal health, dysplasia and malignancy were selected by a non-blinded investigator with more than 20 years of experience in oral pathology and OCT imaging. These images were selected subjectively for being "typical" in appearance for their specific diagnosis, and for excellent image quality. Then these coded OCT images were scored by a blinded visual scorer who had been pre-standardized to 95% agreement with histopathology using 200 standard OCT images with matching histopathological diagnoses from our UCI OCT image database. After completing scoring, the evaluator was unblinded and then provided advice on optical criteria that could be useful to define normative optical characteristics to generate a diagnostic algorithm for distinguishing between healthy, dysplastic and malignant mucosa. Finally, image data was evaluated using a simple image-processing algorithm created in MATLAB.

3.5 Image Processing Methods

Preprocessing of OCT images was necessary as imaging artifacts caused by spherical aberration in the probe design resulted in distorted OCT images shown in Figure 21a. To remove the distorted shape of the oral mucosa an edge detection and flattening algorithm was used[34]. OCT images were then classified as normal, dysplastic, and malignant through a two-step decision tree. Initially, OCT images were categorized into two categories: non-malignant (normal and dysplastic) vs malignant through a comparison of optical tissue stratification. Subsequently, the "non-malignant" group was broken down into

characterization as either “healthy” or “dysplastic” by observing changes in the linearity of the basement membrane at the epithelium- lamina propria junction.

From a superficial observation, the presence of clear and organized epithelial stratification and boundaries in the OCT images can readily give the viewer a sense of tissue classification regarding “non-malignant” vs “malignant”. In images of non-malignant tissues, these were optically delineated for the epithelium and underlying lamina propria as can be seen in Figure 22a,b. However, in malignant lesions of the oral mucosa, tissue stratification seen in Figure 22c and basement membrane delineation were consistently absent. Based on these observations an algorithm was developed to analyze the depth resolved intensity distribution to distinguish images of non-malignant tissues from those of malignant sites. Firstly, a region of interest (ROI) was selected from the original OCT image. An edge detection algorithm previously developed was applied on the ROI to obtain the edge of the first layer. The tissue under consideration was then flattened to a given height with respect to the edge previously found. After flattening, averaging was conducted across the lateral direction of the image. The intensity of every 5 horizontal B-lines was averaged to smooth out the depth resolved intensity distribution. Finally, the intensity depth distribution was averaged using a 20-point sliding window to remove the small peaks in intensity along the depth direction Figure 21c

Based on the depth resolved intensity distribution, a minimum of two peaks was observed in the non-malignant oral mucosal images, while only one peak was observed in images of

cancerous tissues Figure 21. From this analysis, the number of peaks was identified as primary diagnostic decision criterion. Using this rudimentary algorithm, 10 images each of malignant, dysplastic, and healthy oral mucosa were analyzed.

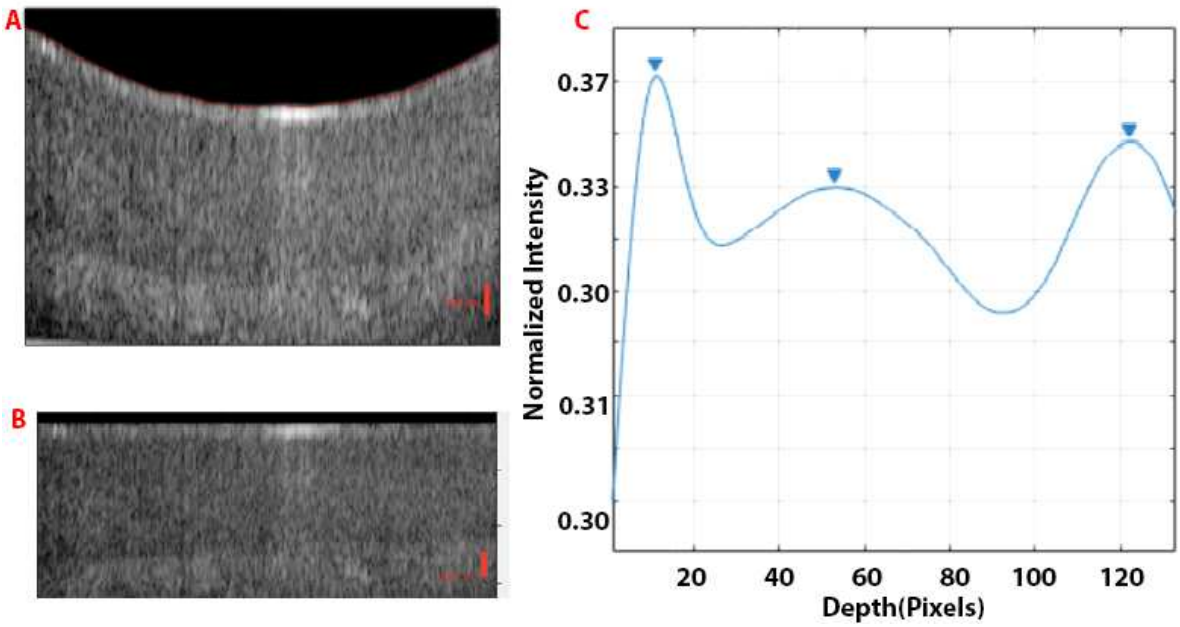

Figure 22 (A) Edge detection with dynamic programming (B) the flattened ROI C) smoothed depth intensity distribution. Scale bars indicate a length of 106µm

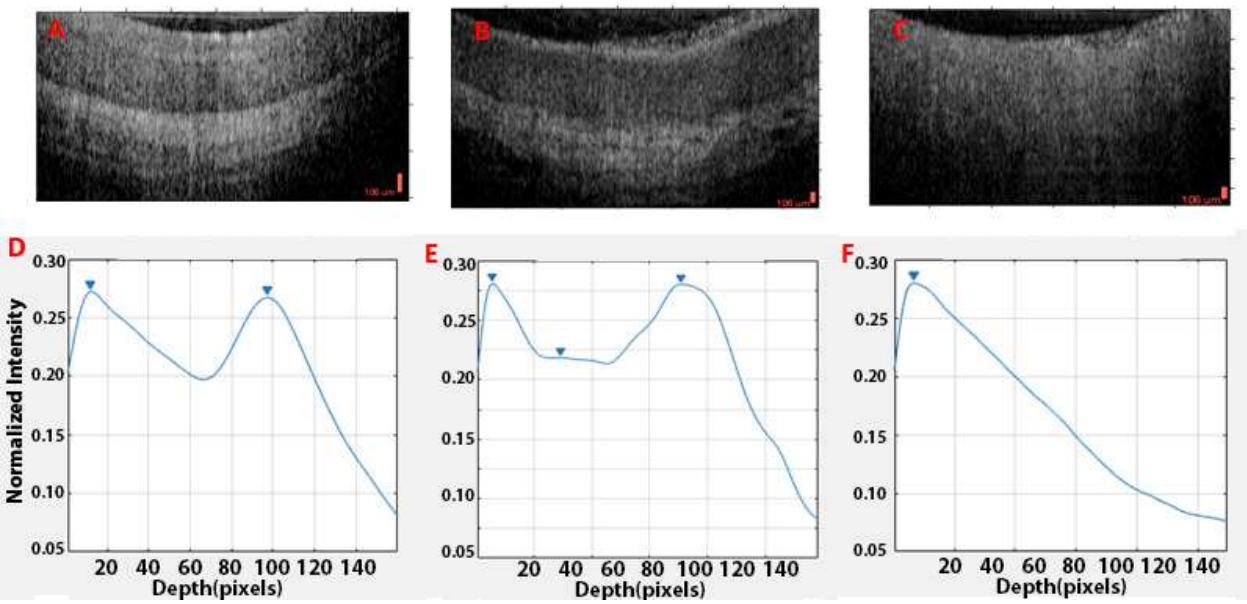

Figure 23 (A)(D) Normal (B)(E) Dysplasia (C)(F) Malignant. OCT image of oral mucosa with corresponding depth resolved intensity

Further differentiation within the "Non-malignant" tissue group to distinguish healthy from dysplastic areas was achieved by evaluating the linearity of the epithelium-to-lamina propria junction seen in the OCT images. During the development and progression of dysplasia, the basement membrane begins downgrowth into the underlying lamina propria. This downward growth is realized as a change in layer morphology in the OCT images from a relatively flat line to a series of localized curved surfaces Figure 23a, b. Thus, the images of non-malignant oral tissues were analyzed for vertical deviation in the epithelium/lamina propria boundary. From the flattened images previously described, the algorithm prompts the selection of an ROI that covers the boundary of the epithelium and lamina propria. The area is then subjected to a previously describe edge detection algorithm to outline the epithelium-lamina propria boundary. The average value in height of this now detect edge is calculated to observe the deviation of the line from a flat linear fit. The absolute value of the deviation from the average height position of the edge is calculated for all points across the

edge and averaged. This was the reported value used to determine how much deviation was present to differentiate dysplastic vs healthy tissues.

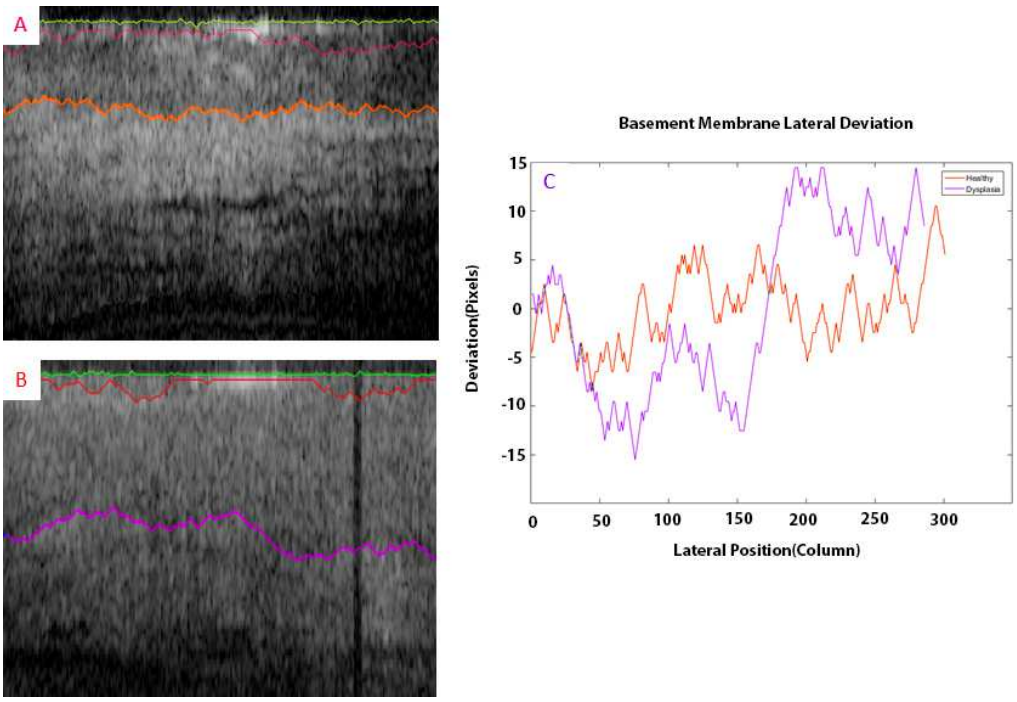

Figure 24 (A,B) Segmented healthy and dysplasia tissue, respectively. Epithelial-lamina propria junction denoted in blue (C) Epithelial-Lamina propria boundary lateral deviation with respect to layer average height.

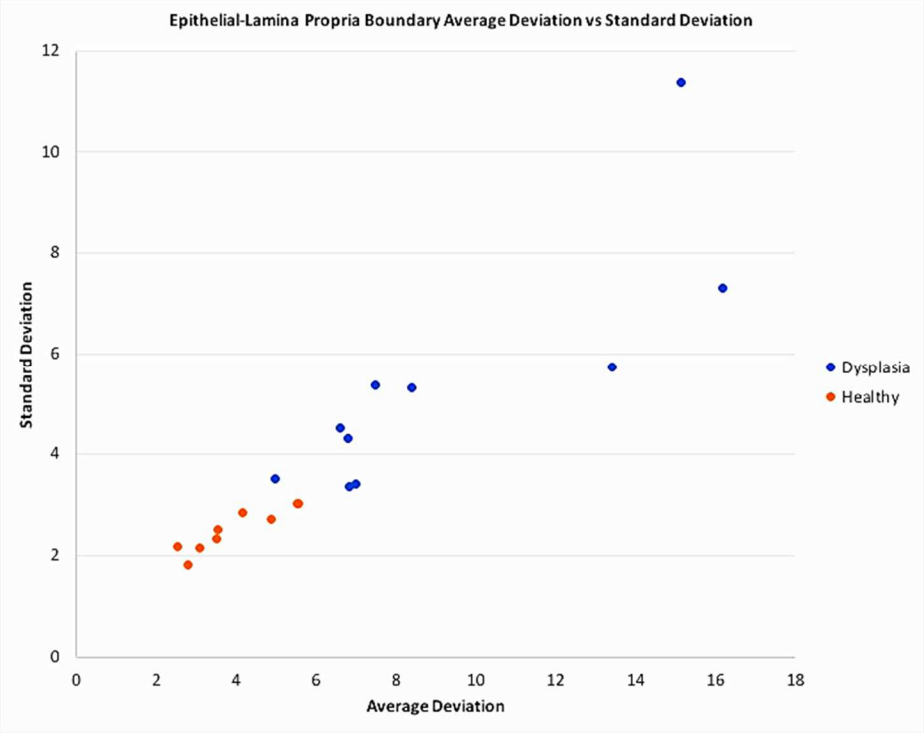

Figure 25 Scatter plot showing separation between health and dysplastic OCT images based upon the average deviation of the epithelial-lamina propria junction and the standard deviation of the distribution of deviations per boundary

3.6 Results and Discussion:

Malignant and pre-malignant or healthy lesions were classified based on the number of peaks identified in the depth resolved intensity distribution. It was found that a minimum of two peaks were observed in the non-malignant oral mucosal images, while only one peak was observed in images of cancerous tissues presented in Fig. 23(c). From this analysis, the number of peaks with a threshold of two peaks were identified as primary diagnostic decision criterion between cancerous and potentially pre-malignant. The loss of heterogeneity between potentially pre-malignant lesions and cancer agrees well with previously published work.

Pre-malignant or dysplastic and healthy OCT image classification was achieved through the previously discussed epithelial-lamina propria boundary deviation. As can be seen in Fig. 25, the dysplastic and healthy OCT image data is well separable using the average deviation and edge standard deviation parameters. An average deviation value of 6 provided a sensitivity and specificity of 90 and 100% for the classification between dysplastic and healthy OCT images. The average deviation values for the dysplastic and healthy group provided statistical significance in a student t-test with a p-value of 0.00012. When considering the standard deviation of the distribution of deviations, a standard deviation of 3.3 provided a sensitivity and specificity of 100 and 90% respectively. The standard deviation values for the dysplastic and healthy group also were statistically significant with a p-value of 0.005.

Diagnostic agreement with the histopathological gold standard was determined through the cohen kappa coefficient of agreement(κ) as well as diagnostic PPVs, NPVs, sensitivity and specificity for the diagnostic classifications of the clinical scorer and algorithm. The results are summarized in Table 2.

Table 2 Sensitivity, Specificity, NPV, PPV and Cohen kappa coefficient of agreement for the clinical observer and diagnostic algorithm to differentiate healthy vs. cancer/dysplasia as well as cancer vs. dysplasia.

	Clinical Observer					**Diagnostic Algorithm**				
	Sens	**Spec**	**PPV**	**NPV**	**κ**	**Sens**	**Spec**	**PPV**	**NPV**	**κ**
Healthy vs.Cancer/Dysp	89%	100%	1	0.83	0.90	95%	100%	1	0.91	0.95
Cancer vs. Dysp	91%	89%	0.91	0.89	0.89	91%	100%	1	0.89	0.90

Diagnostic sensitivity and specificity by the visual scorer were accurate most likely due to extensive scorer training and pre-standardization. Because this study was designed to

provide the foundation for developing the basis for a diagnostic algorithm, with the goal of identifying "typical" optical parameters for health, dysplasia and malignancy, only non-ambiguous images (as defined subjectively by a researcher with over 20 years of experience in OCT imaging for oral pathologies) were included in this study. Sensitivity for differentiating between healthy and dysplastic/cancerous tissue via the image processing algorithm out-performed the clinical scorer by 6%. This could be explained by the notion that clinicians may tend to over-diagnose their patients to prevent a missed diagnosis. However, over-diagnosis can lead to unnecessary tissue biopsy, and possibly reduced patient compliance with any future biopsy recommendations for the purposes of surveillance or diagnosis. It also results in unnecessary cost and use of valuable specialist time and resources.

The diagnostic specificity for differentiating cancer and dysplastic tissues for the clinical observer vs the diagnostic algorithm differed by approximately 11%, with the algorithm performing better than the clinical scorer. The reduced accuracy of visual scoring in this context could be attributed to the challenge of identifying the visually less evident changes in the OCT image that are typical for dysplasia vs oral squamous cell carcinoma. These results suggest that the OCT system, probe and image processing methods developed and tested for this study can inform on triage and provide diagnostic guidance when specialists for biopsy and histopathological evaluation are not available. By using a standardized image-processing algorithm with identical work flow between patient's OCT images, the interpretation uncertainty in a clinical observers' diagnosis could be removed to permit qualitative analysis of tissue features that may not be obvious to the naked eye.

Cohen kappa coefficient of agreement(κ), positive predictor values (PPV), and negative predictor values (NPV) were determined for both clinical observer and diagnostic algorithm diagnosis with respect to a gold standard of histopathology. It can be seen Table 1 that the diagnostic algorithm has a higher κ, PPV, and NPV when differentiating both normal from dysplasia/cancerous legions and dysplasia from cancerous legions in comparison to the clinical observer. These results suggest that the diagnostic algorithm could provide a higher level of agreement with the gold standard of histopathology compared to the diagnostic conclusions determined by the clinical observer.

One can observe the diagnostic and screening potential of OCT imaging paired with an image processing algorithm when comparing sensitivity and specificity of other well documented oral cancer screening tests. A conventional method of oral examination (COE), using incandescent light is a long-standing standard method for oral cancer screening[35]. For COE typical sensitivity and specificity measured across multiple large-scale clinical trials measured 85% sensitivity and 97% specificity[35]. The OCT imaging system and image processing algorithm used in this study evidenced better diagnostic performance than COE. Thus, the proposed OCT-based approach can improve the diagnostic accuracy when an oral oncologist evaluates an oral lesion. This positively re-enforces the positive potential that utilizing such an OCT device in practice could provide. Several existing oral cancer screening tests use narrow-emission tissue fluorescence approaches[35]. Typically, their sensitivity is considerably better than their specificity. Two such devices are the VelScope™ and the Identafi™ [35,36] systems. For both systems, the user is required to make a subjective conclusion based on what he/she perceives from the fluorescent images. This in-turn then

creates the need of training a specialist, which would limit the usability of the device in a remote, underserved or non-specialist setting [36,37]. Lastly, a Stanford research group has recently developed Oscan, an illumination attachment for oral cancer screening. The low cost of the Oscan device makes it an attractive option to be used in LMIC health care settings, but poses several limitations previously discussed. Similar to the VelScope device, the Oscan system cannot access the posterior regions of the oral cavity including the oropharynx providing an incomplete screening of oral health.

In contrast to narrow-band fluorescence emission imaging techniques, OCT utilizes a safe, low-power near infrared light source (5mW 1310nm) that does not pose any safety hazards to the physician or patient yet provides comparable sensitivity and specificity. OCT devices, like the probe and system presented in this work, are configurable to specifically image various hard to reach oral regions that are not readily accessible with current fluorescence-based imaging systems. With further improvements in the imaging probe lateral resolution, focus field distortion and machine learning algorithms to classify tissue cancer types, it is likely that an OCT system will provide excellent triage guidance for oral pre-cancer and cancer in non-specialist settings.

3.7 Conclusion:

A mobile OCT imaging platform and scanning probe were developed and deployed at a healthcare center in Bangalore, India. Oral mucosal health was diagnosed by visual analysis of OCT images via a standardized blinded scorer and an image-processing algorithm, with

biopsy and histopathology serving as the gold standard. In this pilot study of 30 patients, similar levels of diagnostic sensitivity and specificity resulted from image analysis by a blinded clinical scorer and a novel diagnostic algorithm. This work suggests that our image processing algorithm and mobile imaging system could provide a useful screening and triage tool for basic level field screeners where specialist expertise and facilities are not available. Future work will focus on improving the imaging speed of the compact low-cost system, and the discriminatory abilities of the image-processing algorithm.

Chapter 4

Optical Coherence Tomography to Assess Hair Loss Disorders

4.1 Introduction

Most types of hair loss fall into two categories: non-scarring and scarring alopecia. The most prevalent type of hair loss in men and women is androgenetic alopecia (AGA), also known as male pattern hair loss (MPHL) and female pattern hair loss (FPHL). Androgenic alopecia presents itself commonly has a receding hair line in men and hair thinning in women as can be seen in Figure 26.

Figure 26 (A) Male androgenic alopecia better known as male pattern baldness presented as a receding hair line (B) Female androgenic alopecia presented as a hair thinning

Androgenetic alopecia is thought to result from increased levels of certain hormones, including androgens in the body over time, which cause matured hair follicles on the scalp to halt hair reproduction and transforms into terminal hair follicles with thick hairs into vellus hair follicles with thin short hairs seen in Figure 27[38].

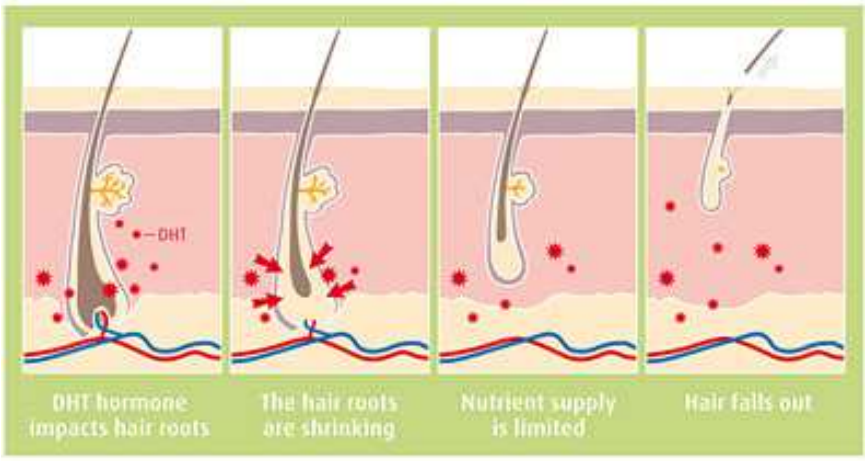

Figure 27 Hair loss process illustrated form the initial effect of DHT hormones on the root of the hair follicle. Over time the hair root shrinks and loses supply with the capillary bed as can be seen in the following panels left to right. Eventually the terminal hair transforms into a vellus hair and is ejected from the scalp as shown in the last frame.

The prevalence of MPHL is highest in Caucasian males and less common in Asian and African-American men. The prevalence of AGA is age-dependent and around 80% and 42% in Caucasian men and women by 70 years of age, respectively [39,40].

The second most prevalent non-scarring alopecia is alopecia areata (AA). Alopecia areata effects roughly 0.1% - 0.2% of the US population and 2% of the world[41]. Alopecia areata lesions usually first appear in the third decade of life and can be located on the scalp, face, or body and undergo spontaneous remission and relapse throughout a patient's lifespan.

Scarring alopecias are a complex group of inflammatory hair loss disorders in which hair follicles are permanently damaged by inflammation in the scalp. Scarring alopecias represent 7.3% of patients who present to specialists for hair loss[42]. These conditions are often rapidly progressive and are very difficult to treat as the pathophysiology is only partially understood.

4.2 Clinical challenges associated with alopecia management

Hair is a central facet of social and psychological well-being. For many, hair represents strength, health, youthfulness, and individuality. Hair loss causes psychological and functional distress, particularly when the conditions are recalcitrant to conventional treatment. Medical treatments for AGA include topical minoxidil, also known as Rogaine, and oral finasteride, a medication that works to block the conversion of undesired androgens. Unfortunately, maintenance of any hair regrowth often requires continuous and indefinite usage of these treatments.

Alopecia areata is treated with a combination of intralesional and topical steroids to decrease scalp inflammation. There are currently no Food and Drug Administration (FDA) approved systemic medications for alopecia areata, however Plaquenil and Methotrexate are frequently prescribed for their systemic anti-inflammatory effects. Additionally, there are several clinical trials investigating the efficacy of a medication approved for use in rheumatologic conditions, janus kinase (JAK)-inhibitors. These medications have shown promising preliminary results in calming autoimmune attack on hair follicles allowing for variable hair regrowth with minimal side effects.

Scarring alopecia is also typically treated with a combination of topical and intralesional medications to decrease scalp inflammation as well as Rogaine. Patients with infectious inflammatory causes of hair loss, such as folliculitis decalvans or dissecting folliculitis, are also managed with appropriate antibiotics. Some people with alopecia may also opt to

explore more final treatment options such as hair transplantation. Efficacy of this procedure in several scarring alopecias has not been shown and is infrequently recommended.

4.3 Current Screening, Diagnostic and Treatment Options for Alopecia

Alopecia is both a clinical and histological diagnosis. Patients are thoroughly examined by a dermatologist, who inspects the patient's scalp for signs of skin irritation, inflammation, scaling, infection, and hair loss. During their examinations, dermatologists will utilize tools such as the pull test and trichoscopy to assess hair follicle vitality and follicular ostia, or openings. Parting the hair in different areas of the scalp can help assess density. Certain distributions of hair loss or hair structures are pathognomonic for certain diseases. For example, hair loss isolated along the frontal hair line with loss of follicular ostia is diagnostic for frontal fibrosing alopecia. It is also important to assess a patient's potential systemic causes of hair loss before establishing a diagnosis. Anemia, nutritional deficiencies, some medications, and hormonal imbalances, such as hypothyroidism, are common causes of diffuse hair loss and must be ruled out with laboratory assessments.

Depending on the medical history of the patient and the onset of hair loss, a biopsy may be required to histologically characterize the scalp tissue as can be seen. The current gold standard biopsy method is a punch biopsy, in which a sharpened cylindrical tool is used to remove a 4-6mm diameter of tissue that is prepared into slides for microscope examination. Horizontal, or transverse, sections of the biopsy yielding the quantity of hair follicles in a specimen is required for the most accurate diagnosis of alopecia that can be seen in Figure 28. Vertical sections of the specimen are also helpful for characterizing the cellular infiltrates

and state of the glandular and neighboring anatomical structures in the dermis for possible pathology[43,44].

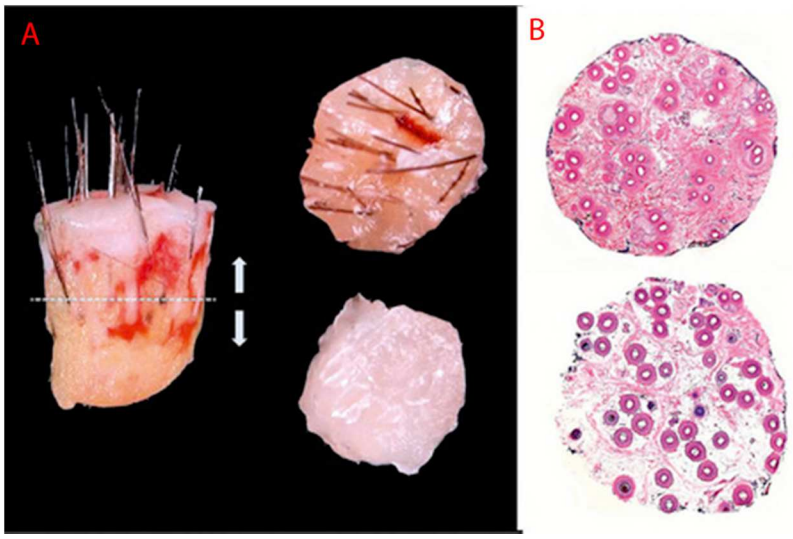

Figure 28 (A) 4mm punch biopsy of human scalp containing epidermis, dermis and subcutaneous fat. The specimen was sectioned into two halves horizontally at the dotted line for further histological sectioning (B) H&E staining of pathology sections from the two halves of the biopsy sample. Hair cross sectional diameter as well as follicular density can be resolved.

Diagnosis of alopecia remains an imperfect practice. Trichoscopy has limited reliability and is somewhat clinician specific. Scalp biopsy remains an invasive procedure with risk of bleeding, infection, and pain, and is associated with challenging processing of the sample taken. Variables such as location of biopsy, technique involved in biopsy and grossing the specimen for microscopic examination are susceptible to human error and variation [44]. Clinicians are not able to monitor the same hair follicles over a disease or treatment course once a collection of follicles is excised.

There is a clinical unmet need to satisfy the shortcomings of the current gold standard. that in-vivo non-invasive means of hair follicles visualization could provide a method of diagnosis

and monitoring for alopecia that decreases pain and delay of diagnosis for patients. OCT a non-invasive imaging modality has been suggested as a potential imaging modality to characterizing hair follicles throughout time as they are affected by immune cells, androgens, or understudied inflammatory processes. OCT is a promising non-invasive imaging modality that has the potential to increase precision in alopecia diagnosis, treatment, and patient satisfaction as well as decrease burden of disease and healthcare cost. To assess the viability of using OCT as a diagnostic screening technique we then conducted an in-vivo feasibility experiment using OCT on scalps degrees of AA.

4.5 Optical coherence tomography as an alopecia screening adjunct

An in-vivo proof-of-principal study was conducted to visualize differences in hair anatomy resolvable in OCT images across normal patients and patients with varying types of AGA. A typical VCSEL-SS-OCT imaging system and forward viewing 2-D scanning probe were utilized to image volunteer scalps. The VCSEL-SS-OCT system was comprised of a 1310nm center wavelength VCSEL with 100nm full width half maximum bandwidth and a 200kHz A-line sweep rate was utilized in a fiber-based Michelson interferometer. The 2-D scanning probe was comprised of a fiber optic collimator, two galvanic scanning mirrors and a scan lens objective providing an axial and lateral resolution of 9μm and 12 μm respectively.

OCT volumetric data was acquired over a 5 x 7mm area on the patient's scalp in affected and normal areas. 1000 OCT B-scan images were acquired in this area giving way to a 7um image spacing. As can be seen in Figure 29 the hair resting on top of the scalp causes a shadow artifact that can allow for measurements of hair diameter. There is a clear distinction between normal healthy hair and thinning hair. Hair diameter was measured off-line using ImageJ (NIMH,

Bethesda, Maryland) where line segments were hand drawn across the hair shadow to determine its length. Normal hair average diameter measured to be 390µm ± 127 µm is presented by the red bars that can be seen in Figure 29A. Miniature hair measured to be 130 µm ± 41.57µm as can be seen in Figure 29B. Normal hair and miniature hair diameters measured showed statistical significance from one another with a t-test p value of 0.00007. Looking into the scalp from the enface perspective seen in Figure 30, one can begin

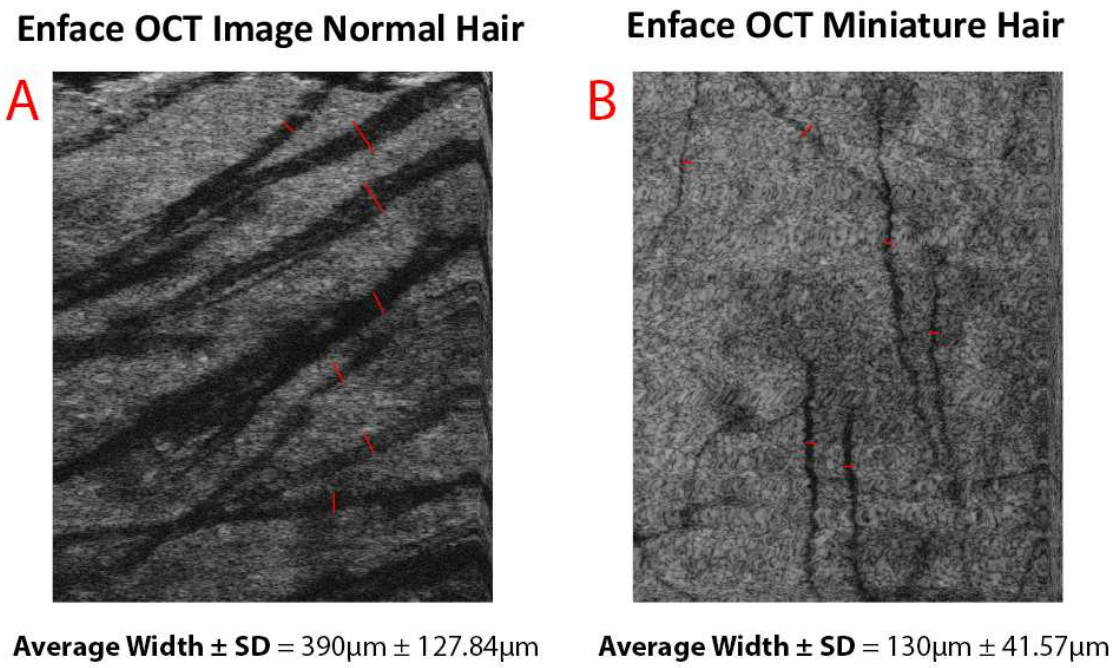

Figure 29 Enface perspective of scalp 3-D OCT image volumes showing hair thickness measured in pixels for (A) normal and (B) miniature hair

to see similar hair shaft and hair follicle structure that can be seen in traditional histological processing. Subsurface hair-shaft and hair-follicle anatomical structure were imaged and assessed off-line using OCT as a proof of concept. Swept Source OCT 3-D B-scans over an area of 6mm x 6mm were acquired for patients of varying diagnosis of androgenic alopecia. Hair follicle and hair shaft structures were visualized in the enface projection of the OCT data as can be seen in Figure 30. The hair follicle observed as the darker region surrounding the brighter hair shaft were

manually segmented in ImageJ. It was found that hair follicle and shaft diameter were larger in areas of healthy hair compared to areas of hair loss area summarized in Table Figure 31. This result agrees well with previous literature that reports a similar finding through histopathological and computer vision segmentation[45].

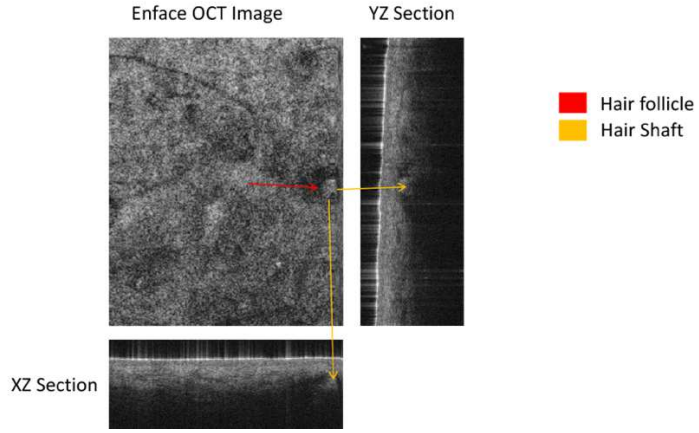

Figure 30 Enface projection of human scalp at a sub-epithelial layer illustrating hair follicle and shaft structures shown in red and yellow respectively.

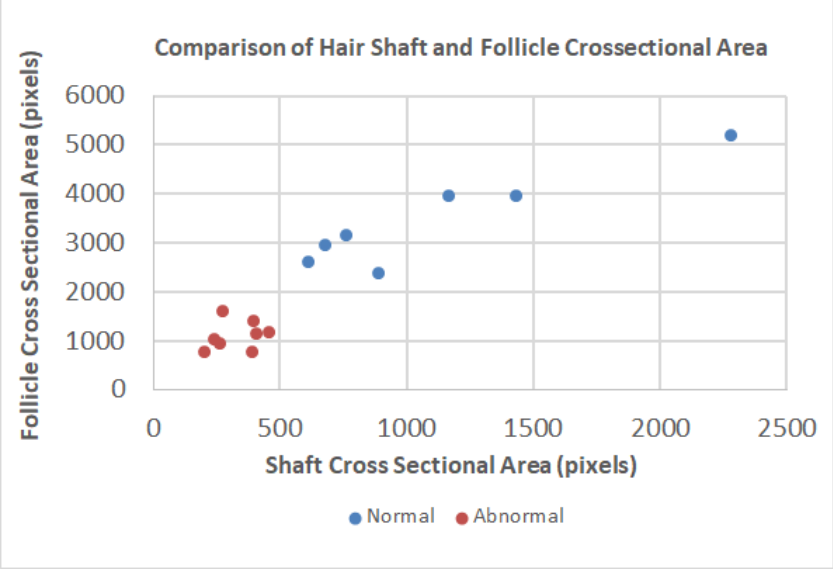

Figure 31 OCT cross-sectional area of shaft and corresponding follicles for normal and abnormal hair growth pathologies

Table 3 Normal and abnormal average cross sectional area measurements for 4 patients with their respetive sample population standard deviation and signitifance.

	Average	Std.	Significance
Normal Shaft*	1116.00	588.07	**0.00241**
Normal Follicle*	3463.14	981.92	**0.00002**
Abnormal Shaft*	328.25	94.58	**0.00241**
Abnormal Follicle*	1107.75	294.56	**0.00020**

***Indicates significance**

4.6 Conclusion:

From the data shown, OCT could potentially be used as a minimally invasive means to assess hair follicle and shaft diameters to characterize varying stages of androgenic alopecia and or the hair growth cycle. Not only can OCT provide similar surface level information of hair diameter and density similar to standard Trichoscopy but provides rich sub-surface hair follicle and hair shaft depth resolved cross-sectional area up to 2mm. Agreeably OCT is limited when used in a patients with thick, fully-grown hair due to the substantial shadowing artifice. However, this patient population is not the target end user for this technology. Future studies planned include using OCT to test the efficacy of hair re-growth experimental methods. Current OCT studies are being conducted using OCT to assess the efficacy of autologous plasma rich platelets sub-cutaneous injections to re-grow hair. Future work also includes further development of a machine learning based algorithm to locate hair follicles with and without a growing hair.

Chapter 5

Conclusion and Future Work

5.1 Measuring Human Anatomical and Physiologic Systems Using OCT

Medical technologic and scientific advancements have permitted a deeper understanding of the pathophysiology of normally functioning and disease states in human tissue. Significant contributions have been made in minimally or non-invasive imaging of biologic tissue specifically but not limited to: X-ray, CT, PET, Ultrasound, MRI and visual endoscopy. In the last 20 years a new era of technologies providing further specific structural data or information, or biochemical activity have surfaced. OCT developed over the last 20 years provides further high resolution detailed tomographic information of which is highly complementary to the scale of ultrasound. Through the body of work in this dissertation I have leveraged the unique property of OCT to provide high resolution tomographic information of biologic scatters to explore new avenues of application of the technology. Specifically, OCT was applied to study pulmonary critical care through the assessment of biofilm growth on the inner lumen of endo tracheal tubes, the study of changes in epithelial mucosa in the development of oral squamous cell carcinoma, and the anatomy of sub surface hair shaft and follicles to better understand AGA. With an understanding of the pathophysiologic changes that are occurring, morphologic information can be extracted from OCT images to further characterize or classify the biologic system. It is this concept of subject quantization that has lead to an on-going future work and mindset that will be implemented in all future work.

5.2 Future Work

The future work of this dissertation is integrate machine learning to develop classification criterion for predicting disease development and onset. In order to achieve this goal one would need to acquire large amounts of labeled image data in the respective physiologic system and then use this data and labels to re-train a pre-existing neural network for classification. Utilizing a trained neural network is particularly important to remove the subjectivity in parameterization of data and classification of data by human scores or observers. As an example, OCT can be integrated in the workflow of suctioning of indwelling endotracheal tubes, such that the respiratory therapist can acquire the data before suctioning. The data acquisition, now integrated into the workflow can be correlated or labeled to the onset of VAP, confirmed by sputum, white blood cell count and fever. The temporal spatial OCT data of the endotracheal tube secretions can then be used to re-train pre-exiting neural network through transfer learning such that the network can accurately predict the onset of VAP from the structure of the biofilm matrix formed. Agreeably, this method may be labor intensive, but it has been shown in literature that re-training a pre-existing network only takes a fraction of the data required to build an entirely new network. In addition, a large patient dataset would eventually be needed by the FDA to validate the use of the technology in-vivo allowing for a natural progression and development of the diagnostic method. As an example for the OCT biofilm pulmonary work, hourly or daily scans of endotracheal tube biofilm can be acquired natively in the workflow of suctioning the mucus secretions on the inner lumen of the ET until the onset of VAP can be recorded. The correlation of the development cycle of bacteria in thickness and the onset of VAP would then be used as a means of a label to re-train the pre-exiting convolutional neural network. As the number of data sets increases the accuracy of the newly trained network will also increase. A non-trivial aspect

of this approach, in this specific example is how to appropriately label the image data prior to the onset VAP. One could claim that the measurement of other parameters such as the white blood cell count, patients oxygenation, and temperature could provide other correlative variables that would aid in such determination. This approach applied broadly across all sub components of this dissertation will transform the use of the OCT in clinical practice from a research tool, to a clinical adjunct that will continually improve with time.

References

1. Pirimoglu B, Sade R, Ogul H, Kantarci M, Eren S, Levent A. How can new imaging modalities help in the practice of radiology? *The Eurasian journal of medicine*. 2016;48(3):213.

2. Huang D, Swanson E, Lin C, … S. Optical coherence tomography. 1991. doi:10.1126/science.1957169

3. Shen K, Lu H, Wang M. Improving lateral resolution of optical coherence tomography for imaging of skins. *International Society for Optics and Photonics*. 2016;9713:97130N.

4. Yaqoob Z, Wu J, Biotechniques Y. Spectral domain optical coherence tomography: a better OCT imaging strategy. 2005.

5. Souza P, Andrade D, Cabral D, Watanabe E. Endotracheal tube biofilm and ventilator□associated pneumonia with mechanical ventilation. *Microscopy Research and Technique*. 2014;77(4):305-312. doi:10.1002/jemt.22344

6. Gil-Perotin S, Ramirez P, Marti V, et al. Implications of endotracheal tube biofilm in ventilator-associated pneumonia response: a state of concept. *Critical Care*. 2012;16(3):1-9. doi:10.1186/cc11357

7. Su J, Zhang J, Yu L, Chen Z. In vivo three-dimensional microelectromechanical endoscopic swept source optical coherence tomography. *Optics express*. 2007;15(16):10390-10396.

8. Jing J, Zhang J, Loy AC, Wong BJ, Chen Z. High-speed upper-airway imaging using full-range optical coherence tomography. *Journal of biomedical optics*. 2012;17(11):110507.

9. Nguyen C, Jung W, Robinson S, Biomedical … AJ. Investigation of Bacterial Biofilms in the Human Middle Ear using OCT Techniques and Acoustic Measurements. 2012.

10. Harris L, Foster S, Mater RR. An introduction to Staphylococcus aureus, and techniques for identifying and quantifying S. aureus adhesins in relation to adhesion to biomaterials: review. 2002.

11. Chi S, Kim T, Park C, and … YJ. Bacterial pathogens of ventilator associated pneumonia in a tertiary referral hospital. 2012. doi:10.4046/trd.2012.73.1.32

12. Bhattacharjee A, Datta R, Gratton E, Hochbaum AI. Metabolic fingerprinting of bacteria by fluorescence lifetime imaging microscopy. *Scientific reports*. 2017;7(1):3743. doi:10.1038/s41598-017-04032-w

13. Digman MA, Caiolfa VR, Zamai M, Gratton E. The phasor approach to fluorescence lifetime imaging analysis. *Biophysical journal*. 2008;94(2):L14-6. doi:10.1529/biophysj.107.120154

14. Crosignani V, Jahid S, Dvornikov AS, Gratton E. A deep tissue fluorescence imaging system with enhanced SHG detection capabilities. *Microscopy research and technique*. 2014;77(5):368-373. doi:10.1002/jemt.22354

15. Yang X, Yang K, Luo Y, Fu W. Terahertz spectroscopy for bacterial detection: opportunities and challenges. 2016.

16. Zhang W, Brown ER, Viveros L, Burris KP, Stewart C. Narrow terahertz attenuation signatures in Bacillus thuringiensis. *Journal of biophotonics*. 2014;7(10):818-824. doi:10.1002/jbio.201300042

17. Yang X, Wei D, Yan S, et al. Rapid and label□free detection and assessment of bacteria by terahertz time□domain spectroscopy. *Journal of Biophotonics*. 2016;9(10):1050-1058. doi:10.1002/jbio.201500270

18. Ferguson B, Zhang X-CC. Materials for terahertz science and technology. *Nature materials*. 2002;1(1):26-33. doi:10.1038/nmat708

19. Vigneswaran N, Williams MD. Epidemiologic trends in head and neck cancer and aids in diagnosis. *Oral and maxillofacial surgery clinics of North America*. 2014;26(2):123-141.

20. Joshi P, Dutta S, Chaturvedi P, Nair S. Head and Neck Cancers in Developing Countries. *Rambam Maimonides Medical Journal*. 2014;5(2):e0009. doi:10.5041/rmmj.10143

21. Bagan J, Sarrion G, oncology JY. Oral cancer: clinical features. 2010.

22. Güneri P, oncology EJ. Late stage diagnosis of oral cancer: components and possible solutions. 2014.

23. of and VA. Prevalence of oral cancer in India. 2015.

24. Who. Control of oral cancer in developing countries. A WHO meeting. *Bulletin of the World Health Organization*. 1984;62(6):817-830.

25. Llewellyn C, Johnson N, Warnakulasuriya K. Risk factors for squamous cell carcinoma of the oral cavity in young people--a comprehensive literature review. *Oral oncology*. 2001;37(5):401-418.

26. Swaminathan R, Selvakumaran R, Cancer … EP. Cancer pattern and survival in a rural district in South India. 2009.

27. Sankaranarayanan R, Anticancer … ME. Head and neck cancer: a global perspective on epidemiology and prognosis. 1998.

28. Cancer incidence in five continents. Volume VIII. *IARC scientific publications*. 2002;(155):1-781.

29. Coelho K. Challenges of the Oral Cancer Burden in India. *Journal of Cancer Epidemiology*. 2012;2012:1-17. doi:10.1155/2012/701932

30. Yao M, Epstein J, Modi B, Pytynia K, Oral … MA. Current surgical treatment of squamous cell carcinoma of the head and neck. 2007.

31. Olivo M, Bhuvaneswari R, Pharmaceutics KI. Advances in bio-optical imaging for the diagnosis of early oral cancer. 2011. doi:10.3390/pharmaceutics3030354

32. Lee L. The physics and technology of diagnostic ultrasound–a practitioner's guide Gill R. High Frequency Publishing, Sydney, Australia, 142 pp, 350+ figures, ISBN …. 2013. doi:10.1002/jmrs.10

33. Wilder-Smith P, Lee K, Guo S, et al. In vivo diagnosis of oral dysplasia and malignancy using optical coherence tomography: preliminary studies in 50 patients. *Lasers in surgery and medicine*. 2009;41(5):353-357.

doi:10.1002/lsm.20773

34. Qi L, Huang S, Heidari AE, et al. Automatic airway wall segmentation and thickness measurement for long-range optical coherence tomography images. *Optics express*. 2015;23(26):33992-34006.

35. Lingen MW, Kalmar JR, Karrison T, eight P. Critical evaluation of diagnostic aids for the detection of oral cancer. *Oral oncology*. 2008;44(1):10-22.

36. Roblyer D, Kurachi C, Stepanek V, et al. Comparison of multispectral wide-field optical imaging modalities to maximize image contrast for objective discrimination of oral neoplasia. *Journal of biomedical optics*. 2010;15(6):066017. doi:10.1117/1.3516593

37. Lane P, Follen M, MacAulay C. Has fluorescence spectroscopy come of age? A case series of oral precancers and cancers using white light, fluorescent light at 405 nm, and reflected light at 545 nm using the Trimira Identafi 3000. *Gender medicine*. 2012;9(1 Suppl):S25-35. doi:10.1016/j.genm.2011.09.031

38. Levy LL, Emer JJ. Female pattern alopecia: current perspectives. *International journal of women's health*. 2013;5:541-556. doi:10.2147/IJWH.S49337

39. HAMILTON J. Patterned loss of hair in man; types and incidence. *Annals of the New York Academy of Sciences*. 1951;53(3):708-728.

40. Gan DC, Sinclair RD. Prevalence of male and female pattern hair loss in Maryborough. *The journal of investigative dermatology Symposium proceedings*. 2005;10(3):184-189. doi:10.1111/j.1087-0024.2005.10102.x

41. Safavi K. Prevalence of alopecia areata in the First National Health and Nutrition Examination Survey. *Archives of dermatology*. 1992;128(5):702.

42. Dahdah MJ, Iorizzo M. The Role of Hair Restoration Surgery in Primary Cicatricial Alopecia. *Skin appendage disorders*. 2016;2(1-2):57-60. doi:10.1159/000448104

43. Efanato C. Histopathology of alopecia: a clinicopathological approach to

diagnosis. *Histopathology*. 2010;56(1):24-38. doi:10.1111/j.1365-2559.2009.03439.x

44. Tailor A, Asher RG, Craig PJ, Groves RW, Fenton DA, efanato C. The current state of play in the histopathologic assessment of alopecia: two for one or one for two? *Journal of cutaneous pathology*. 2013;40(3):298-304. doi:10.1111/cup.12075

45. Lee M-S, Kossard S, Wilkinson B, Doyle JA. Quantification of hair follicle parameters using computer image analysis: A comparison of androgenetic alopecia with normal scalp biopsies. Australas J Dermatol. 1995;36(3):143-147. doi:10.1111/j.1440-0960.1995.tb00956.x